

Stephen F. Austin State University

SFA ScholarWorks

Electronic Theses and Dissertations

12-2018

Physical and Chemical Controls on Suffosion Development in Gypsic Soil, Culberson County, Texas

Jonah Morris

Stephen F. Austin State University, morrisj@jacks.sfasu.edu

Follow this and additional works at: <https://scholarworks.sfasu.edu/etds>



Part of the [Geology Commons](#), and the [Soil Science Commons](#)

[Tell us](#) how this article helped you.

Repository Citation

Morris, Jonah, "Physical and Chemical Controls on Suffosion Development in Gypsic Soil, Culberson County, Texas" (2018). *Electronic Theses and Dissertations*. 220.

<https://scholarworks.sfasu.edu/etds/220>

This Thesis is brought to you for free and open access by SFA ScholarWorks. It has been accepted for inclusion in Electronic Theses and Dissertations by an authorized administrator of SFA ScholarWorks. For more information, please contact cdsscholarworks@sfasu.edu.

Physical and Chemical Controls on Suffosion Development in Gypsic Soil, Culberson County, Texas

Creative Commons License



This work is licensed under a [Creative Commons Attribution-Noncommercial-No Derivative Works 4.0 License](https://creativecommons.org/licenses/by-nc-nd/4.0/).

**Physical and Chemical Controls on Suffosion Development in Gypsic Soil,
Culberson County, Texas**

By

JONAH MORRIS, Bachelor of Science

Presented to the Faculty of the Graduate School of
Stephen F. Austin State University

In Partial Fulfillment
Of the Requirements

For the Degree of
Master of Science

STEPHEN F. AUSTIN STATE UNIVERSITY

(December 2018)

**Physical and Chemical Controls on Suffosion Development in Gypsic Soil,
Culberson County, Texas**

By

JONAH MORRIS, Bachelor of Science

APPROVED:

Dr. Kevin Stafford, Thesis Director

Dr. Melinda Faulkner, Committee Member

Dr. Wesley Brown, Committee Member

Dr. Kenneth Farrish, Committee Member

Pauline M. Sampson, Ph.D.
Dean of Research and Graduate Studies

ABSTRACT

In the Gypsum Plain, suffosion processes have encouraged road failure through dissolution and transport of gypsic soils; however, no prior research has been conducted within the Delaware Basin in regard to these processes. These phenomena were evaluated in both field and laboratory settings in order to assess the parameters of suffosion development associated with Ranch to Market (RM) 652 in Culberson County, Texas, where infrastructure extends across Castile and Rustler strata. Field studies simulated surficial ponding in various gypsic soils and correlated suffosion potential with soil composition and thickness. Soluble fractions of gypsic soils were delineated through geochemical analyses, further expanding upon the soil descriptions published in the Culberson County Soil Survey (USDA, 2013). Suffosion modeling replicated processes observed in the field through repeated infiltration of Dellahunt and Elcor soils—soil piping and subsidence were induced within suffosion models. Lineaments inferred as solutional fractures were delineated using color infrared (CIR) images to determine regional suffosion potential.

Results obtained from this research were used to form a conceptual model of suffosion development in order to better mitigate damage imposed on infrastructure in evaporite karst terrains. Regions with thick, heterogeneous soils of low to moderate gypsum content (10-70%) and moderate fracture densities (100-800 m/km²) are optimal for suffosion development. This model should be considered for future projects in not

only the Gypsum Plain, but for other arid environments with significant evaporite karst and gypsic soils as well.

ACKNOWLEDGEMENTS

Without the help of my thesis advisor, Dr. Kevin Stafford, this study would not have reached its full potential. Thank you for your guidance, patience, and willingness to work with me in the sweltering heat of Texas. I'm also thankful for the Geology Department and the members of my committee who took the time to help me complete this manuscript and guide me through my graduate studies: Dr. Wesley Brown, Dr. Kenneth Farrish, and Dr. Melinda Faulkner. I'm grateful to the Texas Department of Transportation and the West Texas Geological Society for the partial funding that made this research possible. To my friends and colleagues, thank you for all the time and effort spent on helping me finish my field work: Jacob Meinerts, Lillian O'Shay, Jessica Shields, and Sarah Zagurski. Finally, a special thanks goes to my wife, Shannon Morris, for the love and support she's given me throughout my graduate studies.

TABLE OF CONTENTS

ABSTRACT	i
ACKNOWLEDGEMENTS	iii
TABLE OF CONTENTS	iv
LIST OF FIGURES	v
LIST OF TABLES	vii
PREFACE	ix
PHYSICAL AND CHEMICAL CONTROLS ON SUFFOSION DEVELOPMENT IN GYPSIC SOIL, CULBERSON COUNTY, TEXAS	1
ABSTRACT.....	1
INTRODUCTION	3
GEOLOGIC SETTING	7
GYPSIC SOILS.....	10
METHODOLOGY.....	14
RESULTS AND DISCUSSION.....	19
FIELD ANALYSES	19
GEOCHEMICAL ANALYSES	21
SUFFOSION MODELING.....	22
GIS ANALYSES	24
CONCLUSIONS.....	29
REFERENCES	32
APPENDIX A.....	36
VITA.....	60

LIST OF FIGURES

- Figure 1: Study area outlined in black box with general location of Guadalupian and Ochoan strata in the Delaware Basin region and associated geomorphology and surficial hydrology (modified from Stafford et al., 2018)..... 5
- Figure 2: Suffosion features present in the Gypsum Plain including cross-section models on right and field examples on left: (A) Sediments are funneled into an open cover-collapse sinkhole and transported through karstified gypsum bedrock; (B) Lateral soil-piping transports sediments through gypsite macropores; (C) Sediments are transported into solutional fractures widened by gypsite/gypsum dissolution. 6
- Figure 3: A soil map of the detailed soil units derived from the Culberson County Soil Survey (USDA, 2013): BID (Bissett-Rock Outcrop Complex); BIE (Bissett-Rock Outcrop Complex); CVC (Culberspeth-Chilicotal Complex); DEB (Dellahunt Silt Loam); DNB (Dellahunt-Neimahr-Joberanch Complex); ELC (Elcor Gypsiferous Loam); ELE (Elcor Gypsiferous Loam); EPA (Elcor-Dellahunt-Pokorny Complex); EPE (Elcor-Pokorny-Hollomex-Walkerwells Complex); HPC (Hollebeke-Pokorny Complex); MHA (Monohans Fine Sandy Loam); WAB (Walkerwells Silty Clay Loam) ... 13
- Figure 4: Solubility values of gypsite samples collected from field infiltration sites. Filled circles and dashed line represent HCO_3^+ concentrations whereas squares and solid line represent SO_4^{2+} 15
- Figure 5: Piper diagram of gypsite samples collected from field infiltration sites—the point designated by the gray arrow is representative of the Dellahunt soil series and the point designated by the black arrow is representative of the Elcor soil series. Larger points indicate greater TDS (Total Dissolved Solids) values. 16
- Figure 6: Diagram of suffosion modeling and sediment/solute removal: light-gray in the top left cylinder represents water, medium-gray in the bottom left cylinder represents unsaturated gypsite, dark-gray in the bottom right cylinder represents saturated gypsite, and dark grey in bottom right trapezoid represents sediment and saturated fluids transported out of the system as sediment/solute. 17
- Figure 7: Values of soil electrical conductivity and soil moisture both prior (circles) and subsequent (squares) to infiltration studies. The trend line reflects the average increase of soil electrical conductivity as saturation increases ($r^2=0.80$). 20

Figure 8: The results of suffosion modeling with Dellahunt (n=12) and Elcor (n=18) soil models. The left column shows the results of the initial iteration and the right column shows the results of the final iteration. White boxes represent the Dellahunt soil series whereas gray boxes represent the Elcor soil series—median values of each data set are indicated by the horizontal line and averages are indicated by the “x” mark.....23

Figure 9: Orientations of lineaments (n=1159) delineated as solutional fractures proximal to RM 652.....25

Figure 10: Densities of lineaments inferred as solutional fractures in gypsum strata proximal to RM 652. The inset shows CIR imagery with solutional fractures as white lines and sinkholes derived from LiDAR analyses as black polygons.28

Figure 11: A map of regional suffosion potential proximal to RM 652. High potential areas meet all three criteria (moderate infiltration rates, low-to-moderate gypsum content, and moderate fracture densities) whereas low potential areas fail to meet these criteria.31

LIST OF TABLES

Table A-1: Coordinate locations of twenty-five field infiltration sites in the GCS_WGS_1984 coordinate system.	37
Table A-2: Values of soil conductivity, soil moisture, and soil temperature at twenty-five field infiltration sites both prior and subsequent to infiltration.	38
Table A-3: Infiltration rates measured at twenty-five locations within the right-of-way of RM 652.....	41
Table A-4: The initial conditions and results of suffosion modeling with Dellahunt soil models D1-D6 for the first iteration.	47
Table A-5: The initial conditions and results of suffosion modeling with Dellahunt soil models D1-D6 for the second iteration.....	48
Table A-6: The initial conditions and results of suffosion modeling with Dellahunt soil models D1-D6 for the third iteration.	49
Table A-7: The initial conditions and results of suffosion modeling with Dellahunt soil models D7-D12 for the first iteration.	50
Table A-8: The initial conditions and results of suffosion modeling with Dellahunt soil models D7-D12 for the second iteration.....	51
Table A-9: The initial conditions and results of suffosion modeling with Dellahunt soil models D7-D12 for the third iteration.	52
Table A-10: The initial conditions and results of suffosion modeling with Elcor soil models E1- E6 for the first iteration.....	53
Table A-11: The initial conditions and results of suffosion modeling with Elcor soil models E1- E6 for the second iteration.....	54
Table A-12: The initial conditions and results of suffosion modeling with Elcor soil models E7- E12 for the first iteration.....	55

Table A-13: The initial conditions and results of suffosion modeling with Elcor soil models E7- E12 for the second iteration.	56
Table A-14: The initial conditions and results of suffosion modeling with Elcor soil models E13- E18 for the first iteration.	57
Table A-15: The initial conditions and results of suffosion modeling with Elcor soil models E13- E18 for the second iteration.	58
Table A-16: Geochemical data of the soluble fraction of soils from twenty-five field infiltration sites.	59

Physical and Chemical Controls on Suffosion Development in Gypsic Soil, Culberson County, Texas

ABSTRACT

In the Gypsum Plain, suffosion processes have encouraged road failure through dissolution and transport of gypsic soils; however, no prior research has been conducted within the Delaware Basin in regard to these processes. These phenomena were evaluated in both field and laboratory settings in order to assess the parameters of suffosion development associated with Ranch to Market (RM) 652 in Culberson County, Texas, where infrastructure extends across Castile and Rustler strata. Field studies simulated surficial ponding in various gypsic soils and correlated suffosion potential with soil composition and thickness. Soluble fractions of gypsic soils were delineated through geochemical analyses, further expanding upon the soil descriptions published in the Culberson County Soil Survey (USDA, 2013). Suffosion modeling replicated processes observed in the field through repeated infiltration of Dellahunt and Elcor soils—soil piping and subsidence were induced within suffosion models. Lineaments inferred as solutional fractures were delineated using color infrared (CIR) images to determine regional suffosion potential.

Results obtained from this research were used to form a conceptual model of suffosion development in order to better mitigate damage imposed on infrastructure in

evaporite karst terrains. Regions with thick, heterogeneous soils of low to moderate gypsum content (10-70%) and moderate fracture densities (100-800 m/km²) are optimal for suffosion development. This model should be considered for future projects in not only the Gypsum Plain, but for other arid environments with significant evaporite karst and gypsic soils as well.

INTRODUCTION

In northern Culberson County, Texas, dissolution of indurated gypsite (gypsic soil) and gypsum bedrock has caused substantial damage to infrastructure, primarily in the form of road failures (Stafford et al., 2017). The Gypsum Plain of southeastern New Mexico and west Texas (Figure 1) is well recognized for extensive epigene and hypogene karst development, but suffosion processes have become a growing concern related to geohazards in recent years (Stafford et al., 2017). Large sections of Ranch to Market (RM) 652 and other infrastructure within the region have been subjected to road base failure as suffosion piping transports saturated fluids and sediments into underlying karst, predominantly during brief, intense precipitation events. Suffosion is capable of operating at rapid rates in gypsite (Stafford, 2016) and its influence on anthropogenic and environmental regimes may not immediately manifest at the surface. No dedicated studies have been previously conducted of suffosion processes in the Gypsum Plain and it is imperative that methods are developed to evaluate suffosion potential for future construction projects as this region is one of the most rapidly developing petroleum sectors with intense infrastructure usage in North America (Stafford et al., 2017).

Suffosion features are developed by transport of saturated, unconsolidated sediments through soil piping (White, 1988). Laminar transport of fine material through adjacent sediments initiates classic soil piping—pipes spread and connect with underlying karst (Gunn, 2004). Changes in the water table and rapid groundwater flow

can induce collapse by transporting sediments through karstified formations and undermining overlying strata (Palmer, 2007). Flooding of low relief areas promotes subsidence by transporting soil through vertical pipes and fracture zones (White, 1988). Solutional fractures are important for evaporite karst development (White, 1988) and discharge from underlying karst may also cause flooding (Palmer, 2007). Infiltration through thick unconsolidated or allogenic material can induce suffosion depressions (Ford & Williams, 2007), whereas sink-collapse is less probable in thin soils or bedrock (Palmer, 2007). Suffosion processes often influence the development of existing karst features and induce cover-collapse proximal to infrastructure in karst environments (Ford & Williams, 2007).

In the Gypsum Plain, soil caves develop from suffosion (Figure 2) and dissolution of soluble minerals (Stafford et al., 2017). Some soil caves can be laterally extensive and contain isolated chambers several meters in diameter. Preferential flow through indurated soils and evaporite dissolution of the soluble fraction form lateral and vertical soil pipes associated with bedrock solutional conduits and fractures at depth (Stafford et al., 2017). Ascending fluids from Guadalupian aquifers migrate through fractured Castile evaporites (Stafford et al., 2017) and some hypogene features exhibit artesian-like discharge following prolonged precipitation that can be masked by surficial deposits susceptible to suffosion (Stafford et al., 2018).

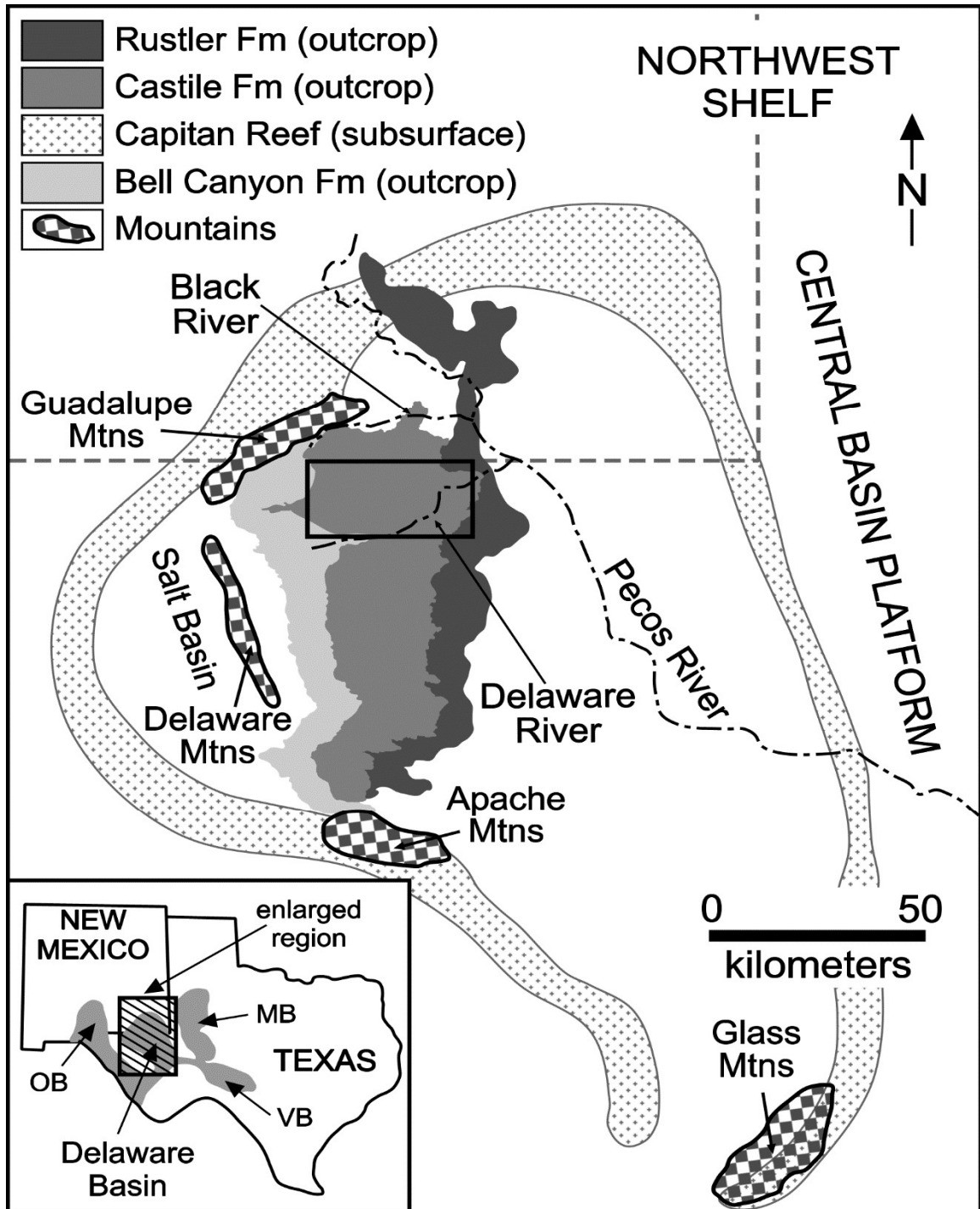


Figure 1: Study area outlined in black box with general location of Guadalupian and Ochoan strata in the Delaware Basin region and associated geomorphology and surficial hydrology (modified from Stafford et al., 2018).

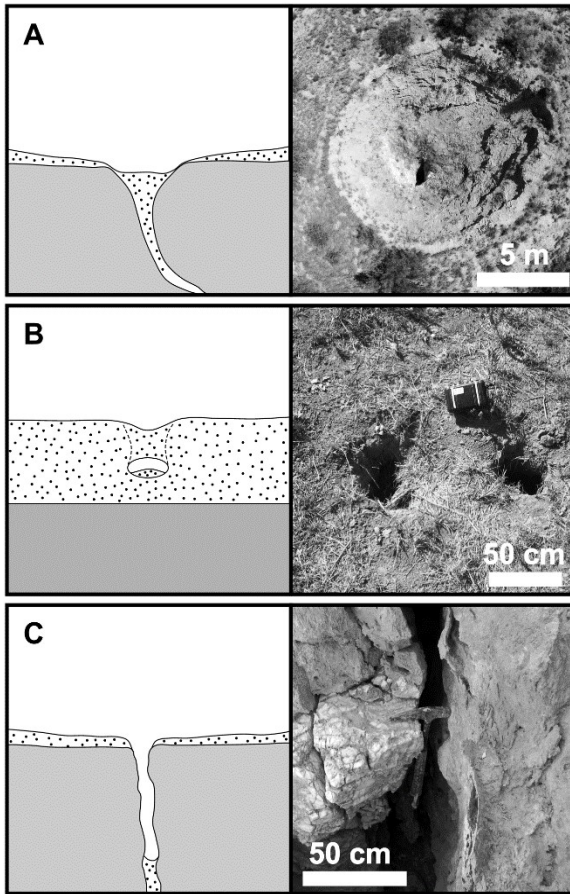


Figure 2: Suffosion features present in the Gypsum Plain including cross-section models on right and field examples on left: (A) Sediments are funneled into an open cover-collapse sinkhole and transported through karstified gypsum bedrock; (B) Lateral soil-piping transports sediments through gypsite macropores; (C) Sediments are transported into solution fractures widened by gypsite/gypsum dissolution.

karst and fractures proximal to infiltration sites. Regional suffosion potential in the

Gypsum Plain may be quantified with an application of the methods introduced below.

Parameters related to suffosion development in gypsite were evaluated in this study along approximately 35 kilometers of RM 652 starting at the intersection of US 62/180 to the west in Culberson County, Texas (Figure 1). This study area was investigated as a proxy for suffosion geohazard development within the greater region as RM 652 bisects the entire Gypsum Plain from west to east. Field-based analyses included infiltration testing coupled with suffosion characterization, including lab-based and remote sensing analyses. Physical

suffosion modelling and chemical analyses of representative gypsite samples were conducted in the laboratory. GIS analyses focused on spatial delineation of evaporite

GEOLOGIC SETTING

Situated between the Delaware Mountains to the west, Rustler Hills to the east, Guadalupe Mountains to the north, and Apache Mountains to the south, the Gypsum Plain is a low relief region that forms the central and western parts of the Delaware Basin (Figure 1). The Delaware Basin formed during the late Paleozoic due to reactivation of Precambrian basement faults and uplift of the Central Basin Platform during the Ouachita Orogeny (Hill, 1996). Precipitation ranges from 20-40 cm/year—most occurs during late summer, intense storm events (Hill, 1996). The Gypsum Plain crops out over ~2,600 km² as Ochoan strata, primarily the Castile Formation (Kirkland & Evans, 1976). Castile evaporites are Late Permian, deep-water, stratified basin deposits (Kendall & Harwood, 1989; Stafford, 2013) that formed as open marine circulation ceased in the Delaware Basin during the late Guadalupian (Hill, 1996). Castile strata are conformable with the underlying Bell Canyon Formation, unconformable with the overlying Salado Formation, and do not extend beyond the basin margins (Hill, 1996). The Castile Formation is massive to laminated gypsum/anhydrite interbedded with halite with extensive intrastratal solutional removal within the western outcrop region (Henrickson & Jones, 1952; Hill, 1996). Castile evaporites increase in thickness from west to east, reaching 480 m thick in the subsurface (Kelley, 1971; Stafford et al., 2008a) with strata dipping 3 to 5 degrees northeast as a result of past tectonism (Hill, 1996).

Evaporite karst development is promoted by high sulfate and halide solubility (Stafford et al., 2008b) which often leads to subsidence, intrastratal collapse and brecciation. Gypsum solubility (2.531 g/L at 20°C) is four orders of magnitude greater than calcite (1.5 mg/L), with more rapid solution kinetics in gypsum than in anhydrite (Klimchouk, 1996). Rock volume increases as anhydrite converts to gypsum; most mature gypsum rocks in near-surface exposures originate from hydration of anhydrite, while sulfate mineral transitions promote development of endokinetic fissuring (Klimchouk, 1996). Anhydrite dominates at depth (>450m) whereas gypsum is most common near the surface (Klimchouk, 1996). Past and present evaporite dissolution affects the entire Delaware Basin, creating a complex speleogenetic history for the region (Hill, 1996). Stafford et al. (2017) classified Castile karst features into the following: intrastratal dissolution, hypogene caves, hypergene caves, and suffosion caves.

Guadalupian siliciclastics provide groundwater that ascends through Castile evaporites and encourages hypogene speleogenesis (Stafford et al., 2018). Intrastratal dissolution forms brecciated structures through hypogene processes coupled with subsequent collapse of evaporite strata (Stafford et al., 2008c). Hypergene caves are small, laterally-limited features with openings that decrease in average cross-sectional area within short distances beyond surface interfaces (Stafford et al., 2017). Suffosion caves are generally too small for human entry (Stafford et al., 2008c), but large soil chambers have been documented that form when connected to larger voids in gypsum bedrock (Stafford et al., 2017). Both natural and anthropogenic sources induce preferential soil piping in the Gypsum Plain (Stafford et al., 2017). The largest karst

features of the Castile Formation developed through hypogene processes at the boundary of the Bell Canyon Aquifer, but most features exhibit variable degrees of epigene overprinting (Stafford et al., 2008b).

Surface drainage is perennial near the Pecos River, semi-perennial near the Black River, and ephemeral at creeks and arroyos (Hill, 1996). The Pecos River flows across the Delaware Basin's backreef, reef, and basin strata, and its tributaries—the Black and Delaware rivers, are contained within the interior of the Delaware Basin (Hill, 1996). The Gypsum Plain's only perennial channel is the Delaware River, but petroleum and ranching operations commonly draw from water sources provided by Quaternary alluvial deposits throughout the region (Stafford et al., 2018). Flash floods are often channeled into arroyos during intense storms (Stafford et al., 2018) and transmitted into the subsurface through evaporite karst interface features (Hill, 1996).

Subsequent to intense precipitation, breached hypogene karst and subsidence valleys overlying fractured bedrock exhibit artesian-like discharge at decadal intervals (Stafford et al., 2018). These conditions are promoted as recharge to the underlying Bell Canyon Aquifer raises the potentiometric surface within the Castile Formation, exceeding the land surface as artesian discharge (Stafford & Faulkner, 2016). Infrastructure in areas with artesian-like discharge are subjected to considerable damage as gypsum laminae are leached from underlying bedrock and overlying gypsic soils are saturated (Stafford et al., 2018).

GYPSIC SOILS

The western outcrop region of the Castile Formation weathers into a dull, gray-white gypsum soil (gypsite) in the Gypsum Plain (Hill, 1996). Gypsite is composed of gypsum and/or anhydrite mixed with insoluble sediments (McGregor, 1954); deposits form as chemical sediments in semi-arid to arid climates (Arakel & McConchie, 1982). Gypsiferous soils result from both physical and chemical vadose diagenesis of existing gypsum strata with subaerial exposure (Arakel & McConchie, 1982). Gypsic crusts develop on exposed bedrock due to repeated gypsum dissolution and reprecipitation (Stafford et al., 2008b).

The change from a cold, humid climate in the Pleistocene to the present arid climate has resulted in the Gypsum Plain's current soil distribution (Hill, 1996; Stafford et al., 2017). Humid conditions brought alluvium to the base of the Delaware Basin; terrace alluvium accumulated in the Pecos River Valley and soil horizons developed in the drier periods (Hill, 1996). Flooding of the Pecos River and its tributaries has distributed graveled alluvium throughout the region (Hill, 1996). These alluvial and gypsic soils overly bedrock in several areas and range from decimeters to several meters thick (Stafford et al., 2017).

USDA (2013) classified soils vary in gypsum content, and textures range from graveled alluvium to gypsiferous loam and fine sand throughout the Gypsum Plain (Figure 3). Soil horizons that contain high gypsum content are generally thin, whereas

low to moderate gypsum content is common in thick, heterogeneous soil profiles. The Bissett-Rock Outcrop Complex (BID) consists of 65% Bissett soils (Lithic Ustic Haplocalcids) weathered from graveled limestone residuum and 25% limestone rock outcrops in areas with 3 to 16% slopes. The Bissett-Rock Outcrop Complex (BIE) in areas with 10 to 30% slopes has a similar composition of 65% Bissett soils and 30% limestone rock outcrops. The Culberspeth-Chilicotal Complex (CVC) consists of 65% Culberspeth soils (Calcic Petrocalcids) weathered from graveled alluvium/colluvium and 30% Chilicotal soils (Ustic Haplocalcids) weathered from graveled limestone pedisidiment in areas with 1 to 8% slopes—this complex is located at the western margin of the study area proximal to BID and BIE complexes. Monohans (MHA) soils (Typic Calcigypsis) form from calcareous and gypsiferous alluvium in areas with 0 to 2% slopes and are proximal to the Delaware River with Walkerwells (WAB) soils (Ustifluventic Haplocambids) derived from alluvial deposits of gypsum and sandstone—gypsum content varies from 0-40%. These soils constitute about 6% of the total study area.

The remaining 94% of the study area is dominated by gypsiferous loams. Dellahunt (DEB) soils (Ustic Calcigypsis) weather from alluvial deposits of gypsum and sandstone in areas with 0 to 5% slopes, and Elcor (ELC/ELE) soils (Lithic Haplogypsis) weather from gypsum residuum in areas with 1 to 30% slopes. The Dellahunt-Neimahr-Joberanch Complex (DNB) consists of 30% Dellahunt soils, 25% Neimahr soils (Lithic Ustic Haplocambids), and 25% Joberanch soils (Ustic Petrogypsis), all of which are weathered from alluvial deposits of gypsum and sandstone. The Elcor-Dellahunt-Pokorny Complex (EPA) consists of 35% Elcor soils, 30% Dellahunt soils, and 25%

Pokorny soils (Ustic Petrogypsid) in areas with 0 to 2% slopes. The Elcor-Pokorny-Hollomex-Walkerwells Complex (EPE) forms in areas with 0 to 30% slopes and consists of 30% Elcor soils, 30% Pokorny soils, 15% Hollomex soils (Ustic Haplogypsid), and 15% Walkerwells soils. The Hollebeke-Pokorny Complex (HPC) consists of 45% Hollebeke soils (Ustic Petrogypsid) and 35% Pokorny soils in areas with 1 to 8% slopes. Undifferentiated gypsiferous loams of the Elcor, Dellahunt, and/or Pokorny soil series contain 60-90%, 0-10%, and 0-95% gypsum content, respectively. However, these soils are undifferentiated as complexes in the soil mapping in ~ 53% of the study area and are effectively inseparable. This variation in soluble fractions inhibits the development of suffosion models for the region from existing soil delineations based on soluble content and complicates geoengineering throughout the region as soil classification is too broadly characterized.

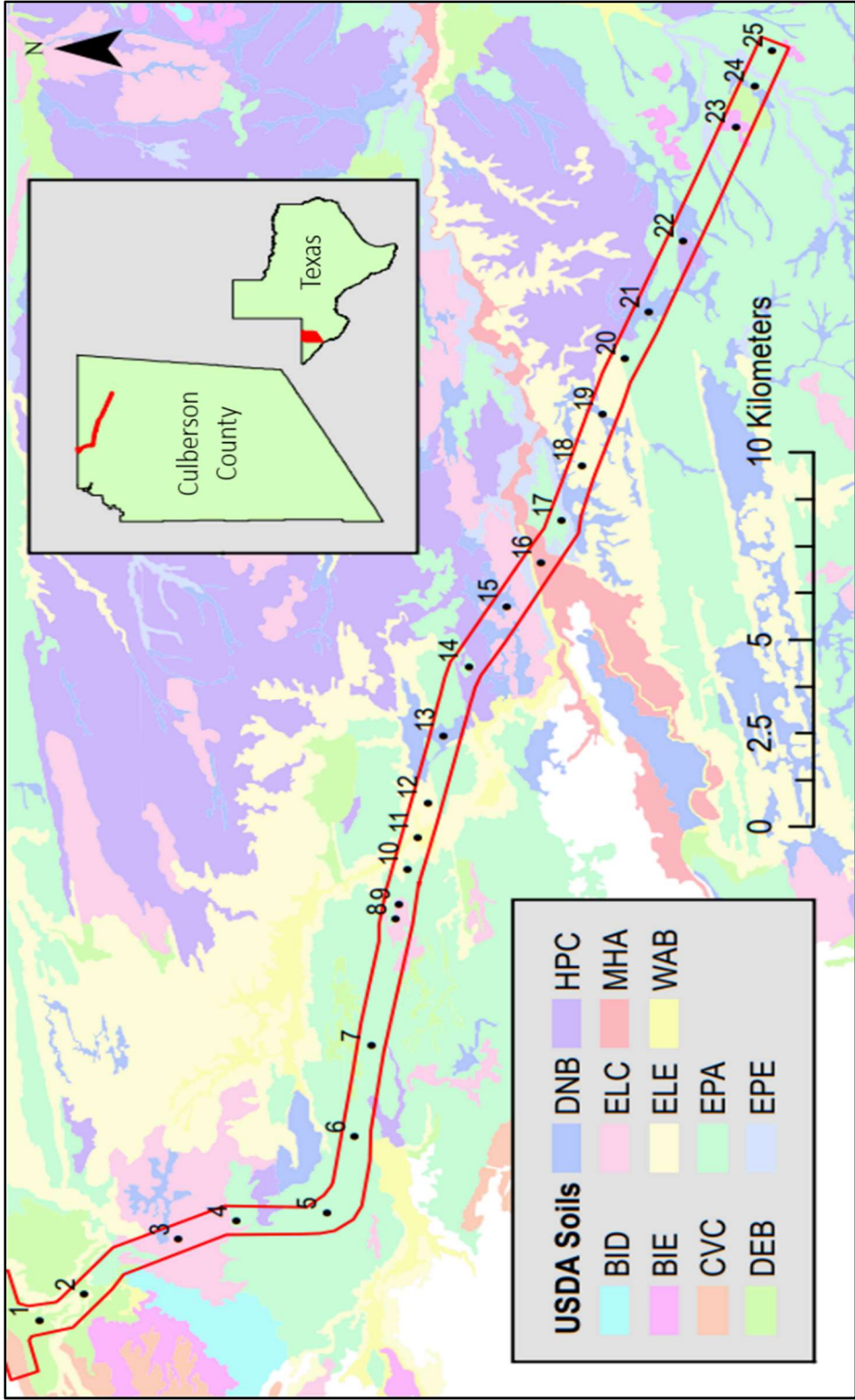


Figure 3: A soil map of the detailed soil units derived from the Culberson County Soil Survey (USDA, 2013): BID (Bissett-Rock Outcrop Complex); BIE (Bissett-Rock Outcrop Complex); CVC (Culberspeth-Chilicotal Complex); DEB (Dellahunt Silt Loam); DNB (Dellahunt-Neimahr-Joberanch Complex); ELC (Elcor Gypsiferous Loam); ELE (Elcor Gypsiferous Loam); EPA (Elcor-Dellahunt-Pokorny Complex); EPE (Elcor-Pokorny-Hollomex-Walkerwells Complex); HPC (Hollebeke-Pokorny Complex); MHA (Monohans Fine Sandy Loam); WAB (Walkerwells Silty Clay Loam).

METHODOLOGY

Combined field and laboratory methodologies were developed to evaluate suffosion processes in the Gypsum Plain. Field studies quantified conditions associated with surficial ponding and infiltration in variable gypsite deposits. Laboratory analyses identified the composition of soluble fractions and composition of gypsic soils. Physical suffosion modeling was designed to replicate suffosion processes observed in field conditions within variable mediums and temporally through repeated infiltration analyses. Delineation of fractures, surficial karst manifestations and regional suffosion potential were conducted through GIS analyses for correlation of observed suffosion phenomena.

Beginning at the intersection of US 62/180, field analyses were conducted at twenty-five locations along the first ~35 kilometers of RM 652 within the Castile outcrop area. Field analyses were conducted over a three-day period without prior precipitation for more than 28 days, and infiltration rates were measured along with soil electrical conductivity, moisture, and temperature. At each site, three Turf-Tec infiltration rings were installed into gypsite deposits within the right-of-way of RM 652 but distal to the road in minimally-disturbed soils—triplicate infiltration analyses were conducted at each infiltration ring site and all infiltration rates were averaged for analyses. GroLine HI98331 EC Tester and Extech M0750 soil moisture meters were used to collect electrical conductivity/temperature and moisture data, respectively. Soil electrical conductivity,

moisture, and temperature were measured at each infiltration ring both before and after infiltration testing. Infiltration rates were correlated to soil classifications designated by USDA (2013) surveys. Soil electrical conductivity was assessed between unsaturated and saturated conditions.

Geochemical analyses were conducted on representative soil samples to delineate soluble fractions (Stafford, 2017). Analysis samples were extracted from well-mixed soils, oven-dried at 40°C until no mass changes were observed to prevent dehydration of gypsum to anhydrite and dissolved in deionized water for 24

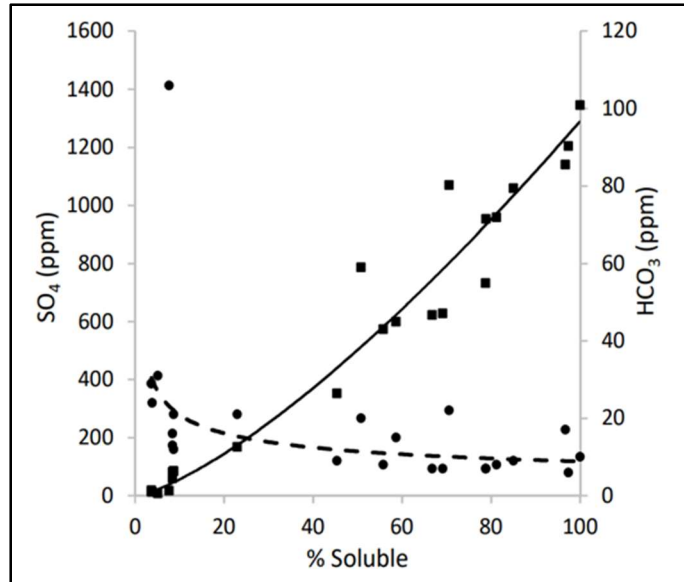


Figure 4: Solubility values of gypsite samples collected from field infiltration sites. Filled circles and dashed line represent HCO₃⁻ concentrations whereas squares and solid line represent SO₄²⁻.

hours with shaker-induced agitation—sample mass was limited to 0.5 g to ensure complete dissolution of soluble minerals (e.g. sulfate minerals) in 250 mL of deionized water. Major cations/anions and TDS were determined from filtered solutions with ICP-MS (Inductively Coupled Plasma Mass Spectrometry) at the SFA Soil, Plant and Water Analysis Laboratory; acid titrations were conducted with a Mettler Toledo EasyPlus Titrator to determine carbonate/bicarbonate concentrations. Geochemical analyses identified three major soil variants based largely on sulfate content (Figure 4): 1) low sulfate content, 2) moderate sulfate content; and 3) high sulfate content.

Suffosion modeling was conducted with bulk samples gathered from Sites 4 and 20. Both gypsite samples are classified by the USDA (2013) as part of the Elcor-Dellahunt-Pokorny Complex (EPA)—these soils constitute 94% of the study area. EPA soils are undifferentiated with gypsum contents that range from 0-95%, thus considerable variation exists between soil compositions (Figure 5). Sites 4 and 20 soils contain 10% and 80% gypsum content, respectively—Site 4 samples represent the

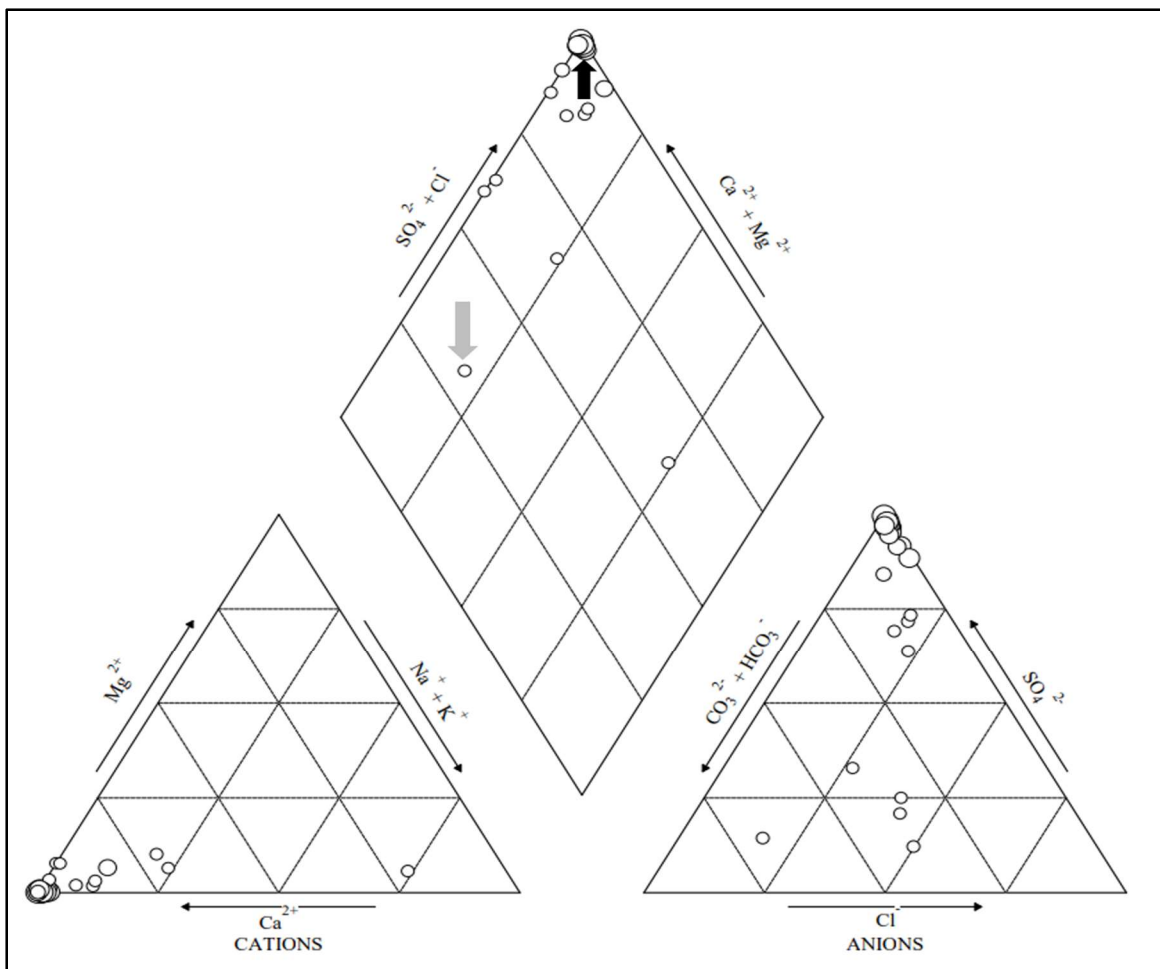


Figure 5: Piper diagram of gypsite samples collected from field infiltration sites—the point designated by the gray arrow is representative of the Dellahunt soil series and the point designated by the black arrow is representative of the Elcor soil series. Larger points indicate greater TDS (Total Dissolved Solids) values.

Dellahunt soil series with low gypsum content (10%) and Site 20 samples represent the Elcor soil series with high gypsum content (>70%).

Physical infiltration modeling was conducted with gypsite that was homogenously mixed and sieved (2 mm) before being packed into butyrate cylinders 10 cm in height and 5 cm in diameter—tubes filled with homogenous soil were percussion-packed with a 1.5kg cylinder dropped twenty times from height of approximately 30cm. Filled cylinders were placed in vertical positions and connected to individual water reservoirs by polyethylene tubing to simulate vadose fluid migration induced by surficial ponding (Figure 6). Water flow was restricted to a maximum rate of 1 mL/s, allowing 100 mL of deionized water

to infiltrate through samples with minimal mechanical mass removal. Fluids and mobilized sediments were gravity-drained through a central exit point 1 mm in diameter into collection containers. Dissolved solids, insoluble sediments and suffosion models were oven-dried at 40°C until no mass change was measured, removing soil moisture without converting gypsum to anhydrite. Drying of sediment-packed columns between infiltration analyses was performed to simulate field conditions where soils are saturated during monsoonal rain events and subsequently dried due to high evaporation in the natural arid environment. Soil mass and volume of suffosion models were measured

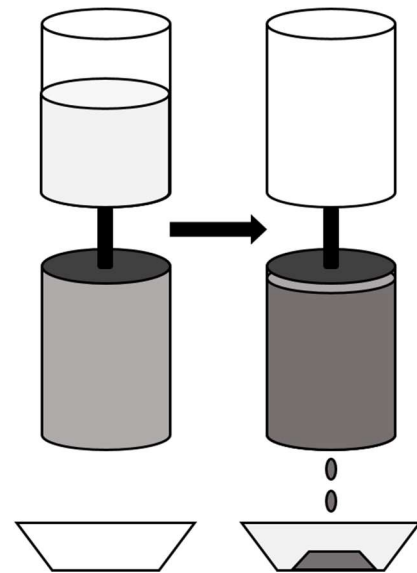


Figure 6: Diagram of suffosion modeling and sediment/solute removal: light-gray in the top left cylinder represents water, medium-gray in the bottom left cylinder represents unsaturated gypsite, dark-gray in the bottom right cylinder represents saturated gypsite, and dark grey in bottom right trapezoid represents sediment and saturated fluids transported out of the system as sediment/solute.

prior and subsequent to infiltration—sediments removed from the system were weighed after the oven-drying phase. Three iterations of this process were conducted with eighteen replicate samples for each soil type (i.e. Dellahunt and Elcor soils).

Raster images with 50 cm resolution were used to map lineaments interpreted as fractures in gypsum bedrock/soil to define potential regions of increased suffosion potential within the study area. Feature selection included lineaments defined by linear vegetative growth (Stafford, 2018) and dismissed features related to anthropogenic activity (i.e. buried utility cables, roads and fences). Lineament orientations and lengths were calculated in ArcGIS and rose diagrams were generated in GeoRose to evaluate spatial variability of fracture intensity. Lineament densities were calculated as line densities in ArcGIS. LiDAR (Light Detection and Ranging) data of sinkhole delineation conducted by Ehrhart (2016) were coupled with mapped lineaments and used to examine suffosion potential correlated with karst conduits in soils associated with infiltration field sites. Ehrhart (2016) delineated natural sinkholes with depths greater than 10 cm by using LiDAR data with a horizontal resolution of 30 cm and vertical resolution of 10 cm—anthropogenic features were manually removed from the data set. Sinkhole densities were calculated as kernel densities in ArcGIS.

RESULTS AND DISCUSSION

Suffosion potential was measured according to physical and chemical parameters evaluated in representative samples of gypsic soil. Field analyses demonstrated the relationship between suffosion potential and soil thickness/type. Geochemical delineation of gypsic soils further characterized the broad soil descriptions published in the Culberson County Soil Survey (USDA, 2013). Suffosion modeling correlated suffosion potential with the soluble/insoluble fractions of gypsite. Fracture and sinkhole delineations were coupled with soil thickness to analyze suffosion potential on a regional scale.

Field Analyses

Field infiltration sites were located within the following USDA (2013) designated soil types: 2 sites in DEB; 3 sites in DNB; 4 sites in ELC; 2 sites in ELE; 11 sites in EPA; 1 site in HPC; 1 site in MHA; and 1 site in WAB (Figure 3). Soils that contain the Elcor, Dellahunt, and/or Pokorny series dominate the study area—these gypsiferous loams constitute ~94% of total area. The highest (4.7 mm/min) and lowest (0.5 mm/min) infiltration rates were measured from DEB and MHA soils, respectively. DEB soils are moderate alkaline silt loams formed from gypsum rock and sandstone, whereas MHA soils are moderate alkaline fine sands derived from calcareous and gypsiferous alluvium (USDA, 2013). The remaining sites (88%) shared an average infiltration rate of ~1.4 mm/min. Moderate to high infiltration rates were observed in thick, heterogeneous soil

mixtures whereas infiltration was limited in thin, fine soils overlying bedrock. Indurated gypsite promoted horizontal infiltration as fluids came into contact with underlying gypsite cements, and heterogeneous soils allowed vertical infiltration in the absence of high soluble fractions. At Site 11, active suffosion was induced as several liters of water infiltrated through a previously unknown

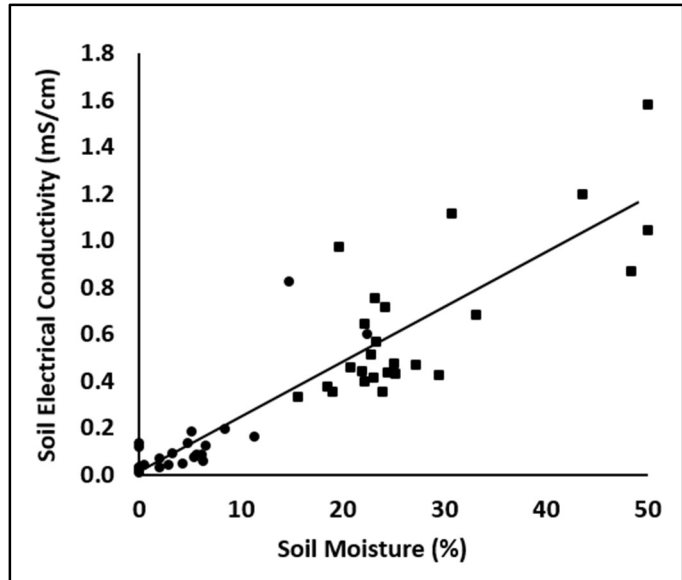


Figure 7: Values of soil electrical conductivity and soil moisture both prior (circles) and subsequent (squares) to infiltration studies. The trend line reflects the average increase of soil electrical conductivity as saturation increases ($r^2=0.80$).

macropore during infiltration testing, forming a “whirlpool” as sediments were flushed into the subsurface, while other infiltration rings within one meter exhibited slow infiltration rates thus indicating the potential for extreme local heterogeneity of suffosion phenomena and permeability. Suffosion geohazards are more probable in thick, heterogeneous soils that promote moderate infiltration.

Soil electrical conductivity and moisture values were low prior to infiltration, ranging from 0.0 to 0.25 mS/cm and 0 to 10%, respectively. Most soil moisture readings increased beyond 20% during infiltration and all soil electrical conductivity readings surpassed 0.25 mS/cm (Figure 7). These increases indicate that infiltrated fluids reached near saturation with respect to sulfate in gypsite deposits and that soluble ions were quickly mobilized. Areas where soil moisture increased beyond 40% exhibited gypsite

compositions with significant clay content that favored soil swelling over vertical infiltration. A direct correlation exists between soil electrical conductivity and moisture throughout the study area, suggesting that moisture content is directly associated with clay content—organic content is extremely low in most soil series within the Gypsum Plain.

Geochemical Analyses

Over 70% of soluble fractions in most soils within the study area are composed of gypsum, but some chloride and carbonate minerals are present (Figure 5). Generally, chloride and carbonate ions in the study area are most concentrated near the surface due to dissolution and vertical transport of calcium sulfates into deeper soils or speleogenetic features. Calcium sulfates are also leached at depth when coupled with karst features. TDS (Total Dissolved Solids) of soils indicate solubilities exceeding 80% within the region with greater concentrations of soluble fractions at depth.

Soils in the study area can be grouped into three classifications based on their geochemical compositions: fluvial deposits, graveled alluvium, and gypsiferous loams. Sediments deposited by the Delaware River (fluvial deposits) exhibit the lowest soluble sulfate composition (<10%) and total solubility as a result of flooding and surface flow through unconsolidated deposits. Graveled alluviums at the western and eastern edges of RM 652 also have low solubilities and greater chloride/carbonate (>50%) concentrations—these soils are weathered from limestone transported by the Black River. Gypsiferous loams contain the highest concentrations of calcium sulfates (>50%), but varying amounts of chloride and carbonate minerals are present. Greater

concentrations of carbonate/chloride ions are generally in gypsiferous loams with thick soil profiles that are proximal to fluvial deposits. Mixing of alluvial and gypsic soils form heterogeneous mixtures that promote infiltration and dissolution of soluble fractions (gypsum). Soils with almost 100% calcium sulfate compositions appear to be derived in situ from underlying gypsum bedrock and form as thin, indurated gypsite that reduces infiltration and ion mobilization.

Suffosion Modelling

In general, suffosion models exhibited considerable increases in bulk density between initial conditions and the first iteration of infiltration—Dellahunt models increased in density by ~12% and Elcor models increased by ~11%. Dellahunt models transported greater amounts of sediment than Elcor models, but greater consolidation was observed in samples from Elcor soils. Porosities increased (1%) in Dellahunt models as infiltration was repeated whereas Elcor models decreased (3%) in porosity with repeated infiltration.

During the first infiltration iteration, Dellahunt and Elcor suffosion models exhibited consolidation and mass removal as deionized water flowed through the system (Figure 8). Some dissolved solutes were removed from the system with insoluble fractions, but most were redistributed during infiltration and cemented around grains after oven-drying, occluding pore space. Consolidation continued in Dellahunt models with replicate infiltration analyses producing little decrease in porosity, indicating that micro-conduits formed during the subsequent iterations—mass removal decreased due to secondary grain cementation. Minimal increase in consolidation paired with decreased

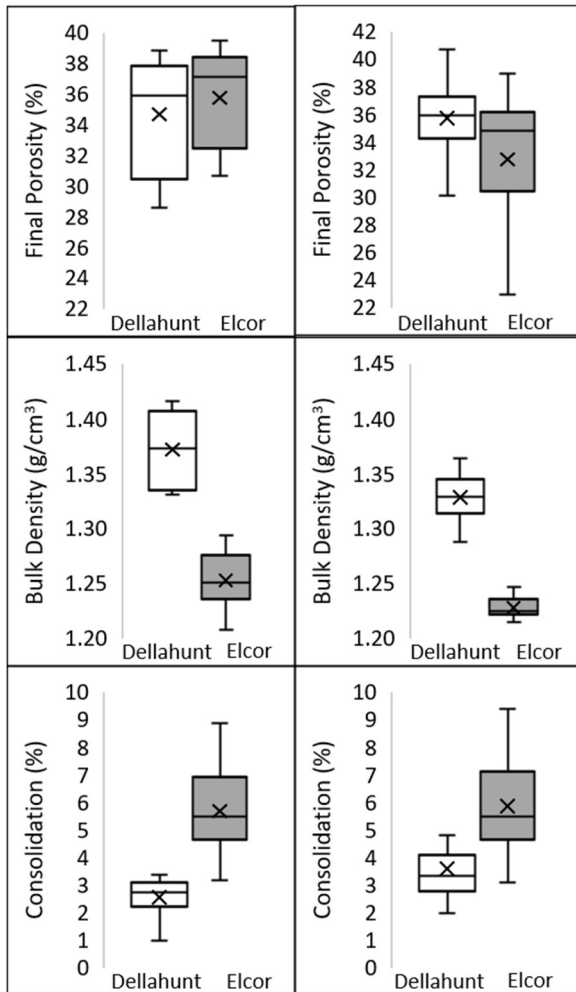


Figure 8: The results of suffosion modeling with Dellahunt (n=12) and Elcor (n=18) soil models. The left column shows the results of the initial iteration and the right column shows the results of the final iteration. White boxes represent the Dellahunt soil series whereas gray boxes represent the Elcor soil series—median values of each data set are indicated by the horizontal line and averages are indicated by the “x” mark.

porosity indicates that fluids were not able to readily migrate through Elcor models during the replicate infiltrations as permeability was reduced. Precipitated gypsum removed initial porosity as models were dried.

Dellahunt soil permeability decreased with repeated infiltration modeling but soils developed connected micro-pores coupled with cemented horizons that restricted vertical fluid flow as a result of relocation and precipitation of gypsum. This was evident from increased porosity and decreased consolidation between infiltration iterations

and observable micro-conduits, which would provide inception horizons for suffosion piping. Infiltration ceased due to consolidation and gypsum reprecipitation after repeated iteration

modeling in Elcor soils. Increased consolidation removed porosity between insoluble grains; reprecipitation removed secondary porosity formed by dissolution in the initial iteration.

Modeling demonstrated that suffosion processes are dependent on geochemical variations in gypsite. Dellahunt soils were more effective than Elcor soils in transporting sediment through suffosion processes. Dissolution of soluble fractions promote soil pipe formation, but adequate insoluble material is needed to structurally support conduit permeability. In addition, excessive evaporite content reduces porosity as sulfates are redistributed around insoluble grains and conduits in repeated wetting/drying phases as is common in arid environments. Although suffosion processes are encouraged in gypsite with low to moderate soluble fractions, Elcor samples experienced considerable, rapid consolidation and reflected compositions that favor general subsidence. Geohazards related to suffosion most likely result from a combination of both processes, but models indicate that the development of macropores within indurated gypsite is essential for continued suffosion and the development of potential geohazards.

GIS Analyses

Suffosion features in the Gypsum Plain occur through a combination of physical piping of unconsolidated sediment and dissolution of soluble soil fractions, but soil pipes are not the sole mechanisms of creating suffosion geohazards; fractures and sinkholes coupled to soils transport sediment into underlying karst as well (Figure 2) by providing outlets for removal of insoluble sediments and saturated waters. Overland flow during intense precipitation flushes gypsite into void spaces provided by solutional fractures and conduits in gypsum bedrock which form the dominant coupling mechanism for enhanced suffosion development within the Gypsum Plain. Solutional fractures at the

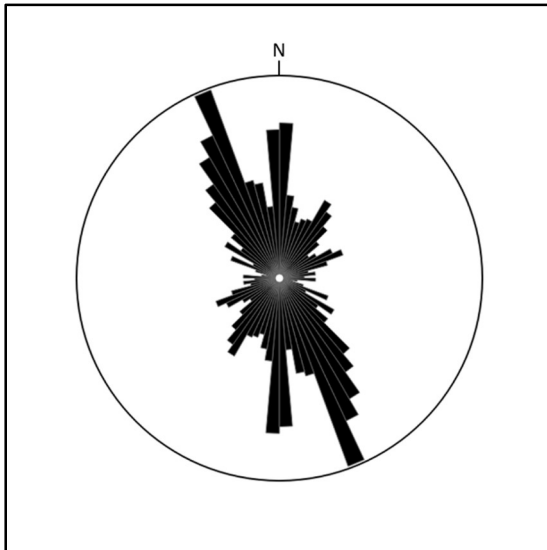


Figure 9: Orientations of lineaments (n=1159) delineated as solutional fractures proximal to RM 652.

contact between gypsum bedrock and gypsic soils have often been correlated with suffosion features proximal to infrastructure in Castile evaporites (Ehrhart, 2016).

Stafford et al. (2017) demonstrated that GIS studies can correlate vegetative growth patterns and available moisture content in evaporite karst environments through CIR (Color InfraRed) and NDVI (Normalized Difference Vegetation Index)

analyses. In this arid environment, linear vegetative growth near fractures in thin soil indicate regions of greater moisture flux—fracture delineation is more difficult in soils with greater thicknesses and more uniform soil infiltration (Stafford et al., 2017). In total, 1,159 lineaments were mapped with general orientations at NW-SE and N-S within the study area (Figure 9). A N-S lineament trend is dominant in the westernmost section of the study area whereas NW-SE trends are observed to the east; similar fracture trends have been observed in caves and subsurface conduits (Stafford et al., 2008c) indicating that these lineaments accurately reflect local fracture deformation.

LiDAR analyses (Ehrhart, 2016) identified the locations of ~ 4,539 natural sinks within the study area—sinkholes are the most prevalent karst landform of the Castile outcrop region (Stafford et al., 2008c) and form due to solutional incision of meteoric water or collapse of strata overlying subsurface voids (White, 1988). Stafford et al. (2008c) concluded that about 55% of sinks within the Castile outcrop resulted from

collapse, whereas the remaining 45% were solutional sinks overprinted by surficial processes. Suffosion processes are capable of operating in all sinks of the Gypsum Plain to some degree because most sinks were filled by gypsite as a result of climate shift from the humid Pleistocene to the arid Holocene. Filled sinks often have conduits obstructed by sediment infilling, allowing for sediment transport without direct observation as meteoric water infiltrates through indurated gypsite or as fluctuations in the water table disrupt sediments and increase drainage. Sinks without open, direct conduits into underlying karst develop suffosion features along permeable interfaces between gypsum bedrock and gypsite as dissolution of soluble fractions redistributes soluble ions and insoluble sediments within features.

Fracture and sinkhole densities correlate well with each other throughout the region (Figure 10). The highest densities are often in areas with exposed gypsum bedrock, whereas lower densities are in thick alluvial deposits or proximal to major fluvial bodies such as the Delaware River. Thin, indurated soils may not promote pipe development, but suffosion processes operate in solutional fractures and sinkholes during intense storms. Sediments are transported beneath the surface as overland flow and shallow vadose flow drains through these suffosion features and open sinks into deeper cavities of Castile evaporites. Water table fluctuations and groundwater flow also remove sediments that restrict sinkhole drainage, allowing suffosion processes to enhance existing collapse structures. However, suffosion potential is greatest in areas with moderate fracture and sinkhole densities. Fractures are most noticeable where soils are thin and bedrock exposed, but moderate fracture densities indicate soil thicknesses

that support soil pipe development. In these areas, suffosion processes operate through all three mechanisms.

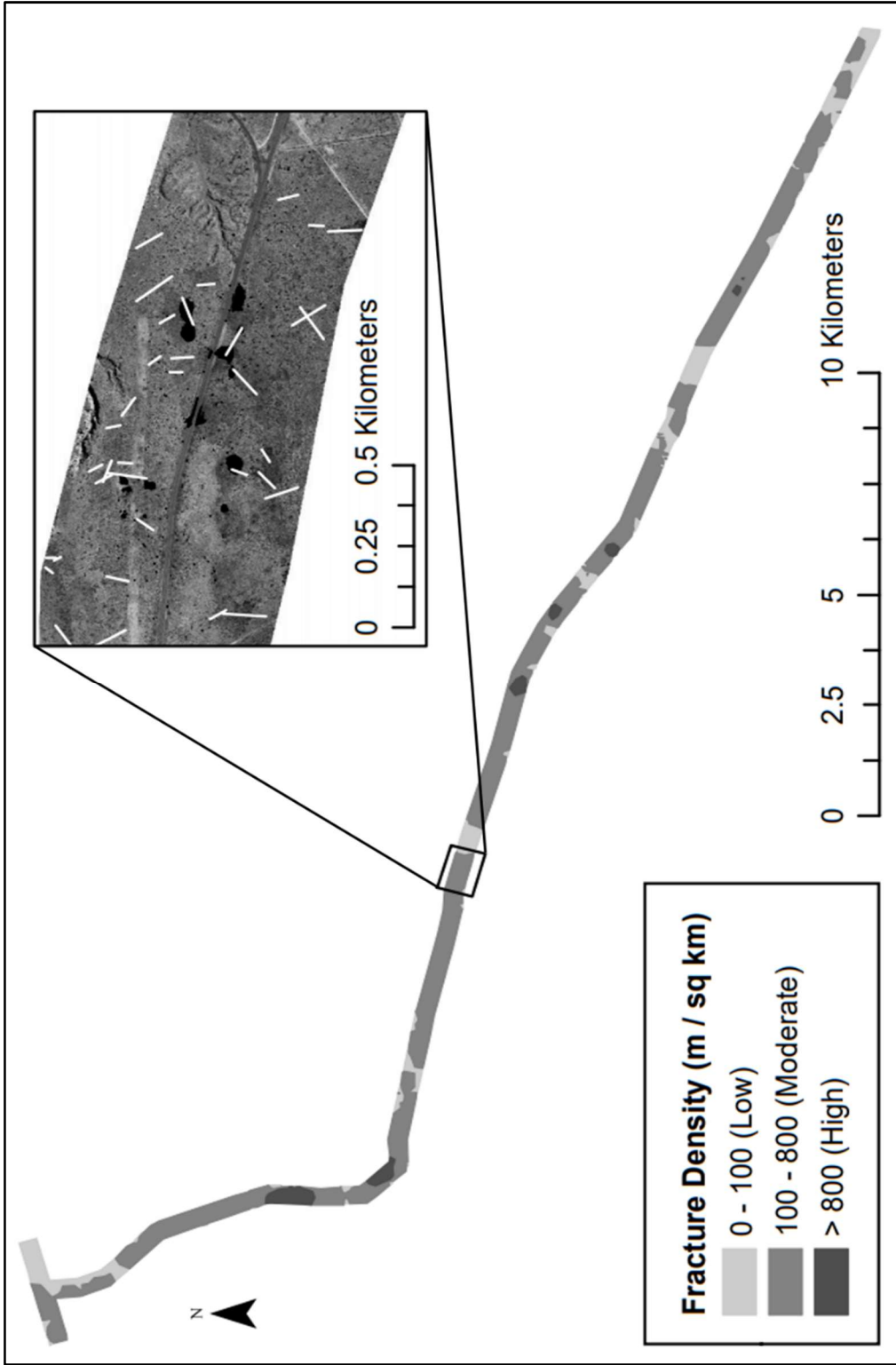


Figure 10: Densities of lineaments inferred as solutional fractures in gypsum strata proximal to RM 652. The inset shows CIR imagery with solutional fractures as white lines and sinkholes derived from LiDAR analyses as black polygons.

CONCLUSIONS

Suffosion features are considerable hazards to infrastructure and human life in the Gypsum Plain and are detrimental to transportation and industry operations. However, combined field and laboratory methods were effective in characterizing suffosion potential in evaporite strata and providing data for improved management of infrastructure in susceptible areas. Suffosion potential in the Gypsum Plain was determined through studies associated with soil composition, soil thickness, and delineation of solutional fractures and evaporite karst.

The compositions of gypsic soils influence suffosion and can be evaluated according to infiltration rates and soluble fractions present. Regions that promote moderate infiltration rates (1.5-2.3 mm/min) are optimal for suffosion development when soluble content is moderate. High infiltration rates remove soluble fractions needed to support conduits formed through soil piping, and low infiltration rates cannot transport insoluble sediment into underlying karst. Soil thicknesses are often related to soil types—heterogeneous mixtures form thick soil profiles whereas thin soils overlying bedrock are high in gypsum and clay content. Soil piping is most effective in soils with low to moderate gypsum content (10-70%) while soils with high gypsum content (>70%) are more inclined toward subsidence through consolidation—further refinement of suffosion potential would be possible with more detailed characterization of soil composition beyond the general, broad characterizations reported by USDA (2013).

Soils with high gypsum content are not preferable for soil piping because of insufficient insoluble sediment needed for the structural support of pipes. Solutional fractures and evaporite karst provide paths for fluid and sediment transport, which thus increase suffosion potential. However, high fracture densities correlate with thin soil cover which precludes suffosion development. Regions with moderate fracture (100-800 m/km²) and karst (100-800 features/km²) densities are most susceptible to suffosion processes because associated soils are thick enough to induce soil piping and are coupled with high permeability bedrock structures. Suffosion potential (Figure 11) is greatest in thick, heterogeneous soils with low to moderate gypsum content (10-70%) and moderate fracture densities (100-800 m/km²).

The methods introduced in this study were economic and effective for discerning areas susceptible to suffosion processes near RM 652, and can be extended to other regions with gypsic soils coupled to evaporite karst. Future construction and mitigation plans should consider suffosion potential when operating in the Gypsum Plain or in areas with significant evaporite karst and/or gypsic soils—delineating suffosion potential can reduce costs for infrastructural maintenance and reduce human endangerment. Field infiltration studies coupled with geochemical analyses provided an effective approach for characterizing soil compositions and thicknesses, while suffosion modeling demonstrated how the ratio between soluble and insoluble fractions of gypsic soils effect suffosion development. Solutional fracture delineation through GIS analyses was useful for determining suffosion potential in sparsely-vegetative areas, and its effectiveness was substantiated through correlation between fracture and evaporite karst

development. It is probable that studies conducted in other evaporite karst environments will produce similar results with the above methodologies

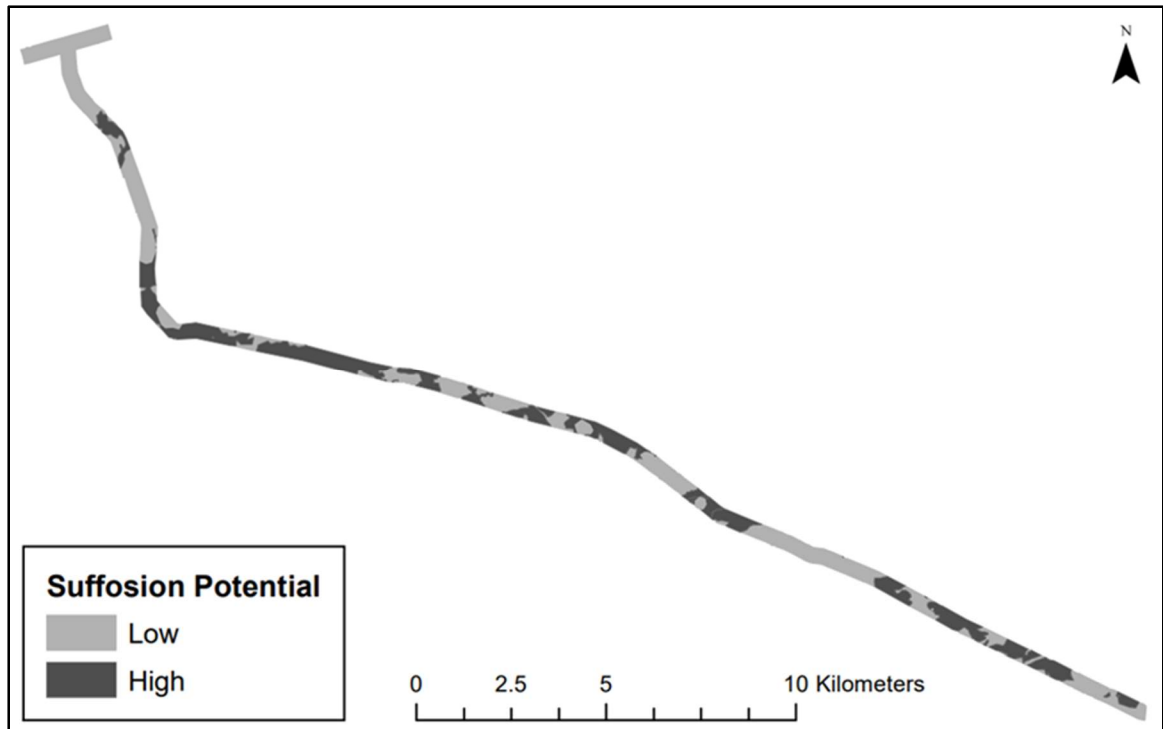


Figure 11: A map of regional suffosion potential proximal to RM 652. High potential areas meet all three criteria (moderate infiltration rates, low-to-moderate gypsum content, and moderate fracture densities) whereas low potential areas fail to meet these criteria.

REFERENCES

- Adams J.E. (1965). Stratigraphic-tectonic development of Delaware Basin: Bulletin of the American Association of Petroleum Geologists, v. 49, 2140-2148.
- Arakel A.V. and McConchie D. (1982). Classification and genesis of calcrete and gypsite lithofacies in paleodrainage systems of inland Australia and their relationship to carnotite mineralization: Journal of Sedimentary Research, 52 (4), 1149-1170
- Barker C.E. and Pawlewicz M.J. (1987). The effects of igneous intrusions and higher heat flow on the thermal maturity of Leonardian and younger rocks, western Delaware Basin, Texas; in Cromwell D.W. and Mazzullo L. (eds.), Glass Mountains: Soc. Econ. Paleontol. Mineral. Guidebook, 69-83.
- Ehrhart J. T. (2016). Speleogenesis and delineation of megaporosity and karst geohazards through geologic cave mapping and LiDAR analyses associated with infrastructure in Culberson County, Texas: Electronic Theses and Dissertations. 66.
- Ford D. and Williams P. (2007). Karst hydrogeology and geomorphology: John Wiley & Sons Ltd, 562 p.
- Gunn J. (2004). Encyclopedia of caves and karst science: Taylor and Francis Books, 902 p.
- Hendrickson G.E. and Jones R.S. (1952). Geology and groundwater resources of Eddy County, New Mexico: New Mexico Bur. Mines Mineral Resources, Groundwater Rept. 3, 109 p.
- Hill C.A. (1996). Geology of the Delaware Basin, Guadalupe, Apache and Glass Mountains: New Mexico and West Texas: Permian Basin Section – SEPM, Midland, TX, 480 p.

- Keller G.R., Hills J.M., Djeddi R. (1980). A regional geological and geophysical study of the Delaware Basin, New Mexico and West Texas: New Mexico Geological Society Guidebook, 31st Field Conference, 105-111.
- Kelley V.C. (1971). Geology of the Pecos Country, Southeastern New Mexico: New Mexico Bureau of Mines and Mineral Resources, Socorro, NM, 78 p.
- Kendall A.C. and Harwood G.M. (1989). Shallow-water gypsum in the Castile Formation – significance and implications. *in* Harris P.M. and Grover G.A. (eds.), Subsurface and outcrop examination of the Capitan shelf margin, northern Delaware Basin. San Antonio (TX): SEPM Core Workshop No 13. 451-457.
- Kirkland D.W. and Evans R. (1976). Origin of limestone buttes, Gypsum Plain, Culberson County, Texas: Am. Assoc. Petroleum Geol. Bull., v. 60, 2005-2018.
- Klimchouk A. (1996). The dissolution and conversion of gypsum and anhydrite: International Journal of Speleology, v. 25, 21–36.
- Lee M.K. and Williams D.D. (2000). Paleohydrology of the Delaware Basin, western Texas: overpressure development, hydrocarbon migration, and ore genesis: Bulletin of the American Association of Petroleum Geologists, 84 (7), 961-974.
- McGregor D.J. (1954). Gypsum and anhydrite deposits in southwestern Indiana: Indiana Department of Conservation, Rept. 8, 24 p.
- Palmer A.N. (2007). Cave geology: Cave Books, 454 p.
- Stafford K. W. (2013). Evaporite karst and hydrogeology of the Castile Formation: Culberson County, Texas and Eddy county, New Mexico; *in* Land L., Doctor D. H., and Stephenson J. B. (eds.), NCKRI Symposium 2: Proceedings of the 13th Multidisciplinary Conference on Sinkholes and the Engineering and Environmental Impacts of Karst, National Cave and Karst Research Institute, Carlsbad, NM, 123-131.

- Stafford K.W. (2016). 2016 Karst Geohazard Characterization of RM 652: Phase Two of Karst Development and Geohazards Associated with RM 652 in Culberson County, Texas: TxDOT rep., 94 p.
- Stafford K.W. (2017). 2017 Karst Geohazard Characterization of RM 652: Phase Three of Karst Development and Geohazards Associated with RM 652 in Culberson County, Texas: TxDOT rep., 45 p.
- Stafford K.W. (2018). 2018 Karst Geohazard Characterization of RM 652: Phase Four of Karst Development and Geohazards Associated with RM 652 in Culberson County, Texas: TxDOT rep., 21 p.
- Stafford K.W. and Faulkner M.S. (2016). Engineering geohazards in hypogene evaporite karst, Castile Formation, west Texas; *in* Chaves T. & Reeling P. (eds.), NCKRI Symposium 6: Proceedings of DeepKarst 2016, origins, resources, and management of hypogene karst, National Cave and Karst Research Institute, Carlsbad, 131-132
- Stafford K.W., Ulmer-Scholle D. and Rosales-Lagarde L. (2008a). Hypogene calcitization: Evaporite diagenesis in the western Delaware Basin: Carbonates and Evaporites, v. 23, 89–103
- Stafford K.W., Rosales-Lagarde L. and Boston P.J. (2008b). Castile evaporite karst potential map of the Gypsum Plain, Eddy County, New Mexico and Culberson County, Texas: a GIS methodological comparison. *J. Cave and Karst Studies*, 83-98.
- Stafford K.W., Nance R., Rosales-Lagarde L. and Boston P. (2008c) Epigene and hypogene gypsum karst manifestations of the Castile Formation: Eddy County, New Mexico and Culberson County, Texas, USA: *International Journal of Speleology*, v. 37, 83–98.
- Stafford K.W., Brown W.A., Ehrhart J.T., Majzoub A.F. and Woodard J.D. (2017). Evaporite karst geohazards in the Delaware Basin, Texas: review of traditional karst studies coupled with geophysical and remote sensing characterization: *International Journal of Speleology*, 46 (2), 169-180

Stafford K.W., Ehrhart J., Majzoub A., Shields J. and Brown W. (2018). Unconfined hypogene evaporite karst: West Texas and southeastern New Mexico, USA: *International Journal of Speleology*, 47 (3), 293-305

United States Department of Agriculture (USDA), Natural Resources Conservation Service (2013). Soil survey of Culberson County, Texas.

White W.B. (1988). *Geomorphology and hydrology of karst terrains*: Oxford University Press, 464 p.

APPENDIX A

DATA INVENTORY

Table A-1: Coordinate locations of twenty-five field infiltration sites in the GCS_WGS_1984 coordinate system.

Site	Latitude (Decimal Degrees)	Longitude (Decimal Degrees)
1	31.99	-104.53
2	31.98	-104.52
3	31.96	-104.51
4	31.95	-104.5
5	31.93	-104.5
6	31.93	-104.48
7	31.92	-104.46
8	31.92	-104.43
9	31.92	-104.43
10	31.92	-104.42
11	31.91	-104.41
12	31.91	-104.4
13	31.91	-104.39
14	31.9	-104.37
15	31.9	-104.36
16	31.89	-104.35
17	31.89	-104.34
18	31.88	-104.32
19	31.88	-104.31
20	31.87	-104.3
21	31.87	-104.29
22	31.86	-104.27
23	31.85	-104.24
24	31.85	-104.23
25	31.85	-104.22

Table A-2: Values of soil conductivity, soil moisture, and soil temperature at twenty-five field infiltration sites both prior and subsequent to infiltration.

Site	Initial Soil Conductivity (mS/cm)	Final Soil Conductivity (mS/cm)	Initial Soil Moisture (%)	Final Soil Moisture (%)	Initial Temperature (C°)	Final Temperature (C°)
1a	0.09	0.50	9.4	35.0	16.5	23.5
1b	0.11	0.43	2.3	32.5	15.6	23.4
1c	0.03	0.35	4.6	21.0	18.7	18.5
2a	0.17	0.38	5.9	22.8	9.3	16.5
2b	0.26	0.43	11.5	23.4	9.5	18.2
2c	0.15	0.43	7.8	22.9	8.6	19.5
3a	0.02	0.50	0.0	31.1	16.5	18.7
3b	0.03	0.44	0.0	25.1	16.0	15.9
3c	0.05	0.46	0.0	25.5	13.4	17.9
4a	0.04	1.01	0.0	50.0	18.2	19.1
4b	0.19	0.89	9.8	50.0	17.6	19.0
4c	0.05	1.23	0.0	50.0	17.5	18.7
5a	0.04	1.27	3.8	50.0	20.0	20.5
5b	0.03	2.51	2.3	50.0	19.7	21.5
5c	0.03	0.96	0.0	50.0	23.2	20.6
6a	0.08	0.49	0.0	28.7	13.0	19.3
6b	0.05	0.38	7.3	23.6	13.9	17.5
6c	0.01	0.20	5.6	19.4	15.1	13.2
7a	0.14	0.66	0.0	23.9	17.6	16.9
7b	0.22	0.78	0.0	25.6	17.4	17.1
7c	0.04	0.71	0.0	23.1	17.0	17.1
8a	0.06	0.40	8.7	24.4	5.8	14.0
8b	0.06	0.42	7.9	24.5	5.5	14.1
8c	0.06	0.49	2.0	24.4	6.5	12.6
9a	0.68	0.92	27.0	45.3	8.3	14.9
9b	0.60	0.84	21.9	50.0	7.1	15.4
9c	0.52	0.85	18.3	50.0	7.1	21.7

Table A-2 (cont.): Values of soil conductivity, soil moisture, and soil temperature at twenty-five field infiltration sites both prior and subsequent to infiltration.

Site	Initial Soil Conductivity (mS/cm)	Final Soil Conductivity (mS/cm)	Initial Soil Moisture (%)	Final Soil Moisture (%)	Initial Temperature (C°)	Final Temperature (C°)
10a	0.01	0.46	0.0	25.3	17.1	20.6
10b	0.03	0.45	0.0	24.0	16.8	19.9
10c	0.04	0.51	0.0	26.0	16.1	19.6
11a	0.12	1.10	13.5	16.2	19.9	17.7
11b	0.13	1.17	9.4	49.9	19.0	18.9
11c	0.24	1.07	10.9	26.0	18.9	18.4
12a	0.02	0.41	0.0	18.3	17.2	17.0
12b	0.00	0.53	0.0	23.0	18.3	17.1
12c	0.00	0.39	0.0	24.3	17.9	17.6
13a	0.10	0.46	0.0	25.0	2.6	15.1
13b	0.11	0.43	8.1	25.0	1.3	15.0
13c	0.05	0.40	8.9	25.5	3.1	13.1
14a	0.05	0.37	0.0	23.4	15.5	15.4
14b	0.05	0.32	0.0	20.1	15.3	15.4
14c	0.03	0.51	8.4	22.8	15.2	14.7
15a	0.22	0.92	14.3	45.2	0.3	1.3
15b	2.04	1.70	16.3	45.1	0.4	0.4
15c	0.22	0.97	13.5	40.4	0.0	0.8
16a	0.07	0.57	2.3	23.5	4.6	5.2
16b	0.03	0.49	2.3	20.6	4.7	5.5
16c	0.10	0.32	1.2	18.2	4.6	5.5
17a	0.40	0.48	3.9	22.9	6.0	4.0
17b	0.09	0.50	4.3	22.3	4.5	4.5
17c	0.07	0.56	7.3	23.2	4.7	4.5

Table A-2 (cont.): Values of soil conductivity, soil moisture, and soil temperature at twenty-five field infiltration sites both prior and subsequent to infiltration.

Site	Initial Soil Conductivity (mS/cm)	Final Soil Conductivity (mS/cm)	Initial Soil Moisture (%)	Final Soil Moisture (%)	Initial Temperature (C°)	Final Temperature (C°)
18a	0.05	0.77	1.5	48.5	0.8	11.3
18b	0.04	0.71	0.0	26.0	0.0	11.2
18c	0.04	0.57	0.0	24.8	0.0	10.5
19a	0.10	0.79	0.0	23.2	1.9	2.4
19b	0.26	0.70	5.8	22.8	1.1	3.4
19c	0.04	0.77	8.5	23.3	0.7	3.7
20a	0.15	0.62	7.9	24.8	7.4	8.1
20b	0.09	0.63	7.9	16.0	7.2	7.9
20c	0.02	0.69	2.5	25.5	5.9	7.9
21a	0.09	0.45	0.0	23.0	7.3	8.0
21b	0.12	0.74	0.0	29.5	6.7	7.5
21c	0.15	0.51	0.0	17.3	6.4	8.0
22a	0.05	0.42	7.4	15.0	1.3	0.3
22b	0.21	0.18	3.8	18.7	0.6	0.3
22c	0.11	2.32	8.4	25.1	1.1	6.2
23a	0.00	0.31	0.0	23.0	6.5	7.7
23b	0.09	0.39	0.0	22.0	3.0	7.7
23c	0.01	0.36	0.0	12.1	3.9	2.5
24a	0.02	0.29	0.0	22.0	1.4	1.4
24b	0.01	0.35	0.0	16.5	0.0	1.2
24c	0.01	0.49	0.0	16.9	0.5	2.3
25a	0.02	0.19	0.0	9.8	0.0	0.1
25b	0.02	0.40	0.0	18.0	0.0	1.4
25c	0.02	0.41	0.0	18.8	0.0	2.6

Table A-3: Infiltration rates measured at twenty-five locations within the right-of-way of RM 652.

Site	Time Elapsed (min)	Water Infiltrated (cm)	Infiltration Rate (mm/min)	AVG Infiltration Rate (mm/min)
1a	15.0	8.0	5.3	5.5
	30.0	15.8	5.3	
	39.9	18.8	4.7	
1b	15.0	10.7	7.1	
	30.0	16.3	5.4	
	44.5	22.4	5.0	
2a	15.0	1.4	0.9	3.9
	30.0	3.3	1.1	
	45.0	4.2	0.9	
2b	15.0	3.3	2.2	
	30.0	6.0	2.0	
	45.0	8.4	1.9	
2c	15.0	7.7	5.1	
	21.2	21.4	10.1	
	30.1	33.2	11.0	
3a	15.0	1.5	1.0	1.1
	30.0	2.2	0.7	
	45.0	4.8	1.1	
3b	15.0	2.3	1.5	
	30.0	3.5	1.2	
	45.0	4.7	1.0	
3c	15.0	1.9	1.3	
	30.0	3.4	1.1	
	45.0	4.1	0.9	
4a	15.0	0.5	0.3	0.5
	30.0	1.2	0.4	
	45.0	1.8	0.4	
4b	15.0	0.9	0.6	
	30.0	2.1	0.7	
	45.0	2.2	0.5	
5a	15.0	0.2	0.1	1.5
	30.0	2.8	0.9	
	45.0	3.0	0.7	
5b	15.0	5.6	3.7	
	30.0	5.7	1.9	
	45.0	7.7	1.7	

Table A-3 (cont.): Infiltration rates measured at twenty-five locations within the right-of-way of RM 652.

Site	Time Elapsed (min)	Water Infiltrated (cm)	Infiltration Rate (mm/min)	AVG Infiltration Rate (mm/min)
6a	15.0	3.1	2.1	2.5
	30.0	5.9	2.0	
	45.0	8.2	1.8	
6b	15.0	5.5	3.7	
	30.0	8.4	2.8	
	45.0	10.9	2.4	
7a	15.0	4.7	3.1	1.4
	30.0	7.5	2.5	
	45.0	10.0	2.2	
7b	15.0	1.4	0.9	
	30.0	2.8	0.9	
	45.0	3.9	0.9	
7c	15.0	1.4	0.9	
	30.0	1.9	0.6	
	45.0	2.9	0.6	
8a	15.0	1.8	1.2	1.6
	30.0	3.0	1.0	
	45.0	5.2	1.2	
8b	15.0	1.7	1.1	
	30.0	2.9	1.0	
	45.0	4.5	1.0	
8c	15.0	4.4	2.9	
	30.0	7.1	2.4	
	45.0	10.2	2.3	
9a	15.0	1.3	0.9	1.6
	30.0	1.8	0.6	
	45.0	2.5	0.6	
9b	15.0	1.2	0.8	
	30.0	2.0	0.7	
	45.0	2.6	0.6	
9c	15.0	5.5	3.7	
	30.0	9.3	3.1	
	45.0	15.8	3.5	

Table A-3 (cont.): Infiltration rates measured at twenty-five locations within the right-of-way of RM 652.

Site	Time Elapsed (min)	Water Infiltrated (cm)	Infiltration Rate (mm/min)	AVG Infiltration Rate (mm/min)
10a	15.0	4.7	3.1	2.4
	24.4	13.7	5.6	
	39.4	15.9	4.0	
	54.4	21.4	3.9	
10b	15.0	2.7	1.8	
	30.0	3.8	1.3	
	45.0	5.1	1.1	
10c	15.0	1.7	1.1	
	30.0	2.0	0.7	
	45.0	4.2	0.9	
11a	15.0	2.1	1.4	0.9
	30.0	2.9	1.0	
	45.0	3.7	0.8	
11b	15.0	1.2	0.8	
	30.0	2.3	0.8	
	45.0	3.7	0.8	
11c	1.3	14.2	110.7	
	2.4	28.4	116.0	
	3.6	42.6	118.4	
12a	15.0	2.2	1.5	2.3
	30.0	3.8	1.3	
	45.0	6.1	1.4	
12b	15.0	6.7	4.5	
	30.0	12.4	4.1	
	45.0	18.9	4.2	
12c	15.0	2.7	1.8	
	30.0	3.2	1.1	
	45.0	4.5	1.0	

Table A-3 (cont.): Infiltration rates measured at twenty-five locations within the right-of-way of RM 652.

Site	Time Elapsed (min)	Water Infiltrated (cm)	Infiltration Rate (mm/min)	AVG Infiltration Rate (mm/min)
13a	15.0	5.7	3.8	2.9
	30.0	10.2	3.4	
	39.4	13.2	3.4	
13b	15.0	4.3	2.9	
	30.0	8.3	2.8	
	45.0	11.4	2.5	
13c	15.0	3.7	2.5	
	30.0	6.8	2.3	
	45.0	10.0	2.2	
14a	15.0	0.9	0.6	0.9
	30.0	1.2	0.4	
	45.0	1.5	0.3	
14b	15.0	2.6	1.7	
	30.0	4.1	1.4	
	45.0	5.5	1.2	
14c	15.0	1.4	0.9	
	30.0	1.8	0.6	
	45.0	2.9	0.6	
15a	15.0	0.5	0.3	0.2
	30.0	0.8	0.3	
	45.0	0.9	0.2	
15b	15.0	0.3	0.2	
	30.0	0.4	0.1	
	45.0	0.7	0.2	
16a	15.0	1.0	0.7	0.5
	30.0	1.5	0.5	
	45.0	1.7	0.4	
16b	15.0	1.1	0.7	
	30.0	1.8	0.6	
	45.0	2.6	0.6	
16c	15.0	0.5	0.3	
	30.0	1.2	0.4	
	45.0	1.4	0.3	

Table A-3 (cont.): Infiltration rates measured at twenty-five locations within the right-of-way of RM 652.

Site	Time Elapsed (min)	Water Infiltrated (cm)	Infiltration Rate (mm/min)	AVG Infiltration Rate (mm/min)
17a	15.0	1.2	0.8	0.9
	30.0	2.5	0.8	
	45.0	3.3	0.7	
17b	15.0	0.9	0.6	
	30.0	1.3	0.4	
	45.0	1.5	0.3	
17c	15.0	2.5	1.7	
	30.0	4.4	1.5	
	45.0	6.0	1.3	
18a	15.0	5.1	3.4	2.2
	30.0	7.5	2.5	
	40.6	10.2	2.5	
18b	15.0	5.3	3.5	
	30.0	7.8	2.6	
	45.0	11.0	2.4	
18c	15.0	1.3	0.9	
	30.0	2.5	0.8	
	45.0	3.6	0.8	
19a	15.0	2.5	1.7	1.2
	30.0	2.7	0.9	
	45.0	3.1	0.7	
19b	15.0	3.8	2.5	
	30.0	4.1	1.4	
	45.0	4.5	1.0	
19c	15.0	2.2	1.5	
	30.0	2.6	0.9	
	45.0	2.7	0.6	
20a	15.0	3.9	2.6	1.2
	30.0	4.5	1.5	
	45.0	5.5	1.2	
20b	15.0	1.3	0.9	
	30.0	2.5	0.8	
	45.0	3.0	0.7	
20c	15.0	1.7	1.1	
	30.0	3.1	1.0	
	45.0	3.6	0.8	

Table A-3 (cont.): Infiltration rates measured at twenty-five locations within the right-of-way of RM 652.

Site	Time Elapsed (min)	Water Infiltrated (cm)	Infiltration Rate (mm/min)	AVG Infiltration Rate (mm/min)
21a	15.0	3.3	2.2	1.7
	30.0	5.9	2.0	
	45.0	9.1	2.0	
21b	15.0	1.5	1.0	
	30.0	2.2	0.7	
	45.0	2.4	0.5	
21c	15.0	3.6	2.4	
	30.0	6.5	2.2	
	45.0	9.7	2.2	
22a	15.0	1.5	1.0	0.7
	30.0	1.8	0.6	
	45.0	2.2	0.5	
22b	15.0	1.6	1.1	
	30.0	1.7	0.6	
	45.0	2.2	0.5	
22c	15.0	0.8	0.5	
	30.0	1.6	0.5	
	45.0	3.7	0.8	
23a	15.0	1.5	1.0	1.2
	30.0	2.2	0.7	
	45.0	3.1	0.7	
23b	15.0	2.5	1.7	
	30.0	5.6	1.9	
24a	15.0	0.8	0.5	0.7
	30.0	1.6	0.5	
	45.0	3.9	0.9	
24b	15.0	1.2	0.8	
	30.0	2.3	0.8	
	45.0	3.9	0.9	
25a	15.0	0.9	0.6	0.5
	30.0	1.5	0.5	
	45.0	1.5	0.3	
25b	15.0	0.6	0.4	
	30.0	1.4	0.5	
	45.0	2.3	0.5	

Table A-4: The initial conditions and results of suffosion modeling with Dellahunt soil models D1-D6 for the first iteration.

Sample	Initial Soil Mass (g)	Water Volume (mL)	Saturated Soil Mass (g)	
D1	237.24	100	305.28	
D2	237.7	100	305.93	
D3	237.69	100	304.03	
D4	237.09	100	304.53	
D5	233.01	100	302.58	
D6	235	100	301.32	
Sample	Initial Soil Volume (mL)	Final Soil Volume (mL)	Dried Soil Mass (g)	Soil Removed (g)
D1	180.96	175.35	237.14	0.22
D2	180.96	179.15	239.01	0.22
D3	180.96	177.88	237.11	0.31
D4	180.96	176.79	237.57	0.29
D5	180.96	175.35	234.53	0.3
D6	180.96	176.43	234.9	0.23
Sample	Final Porosity (%)	Final Bulk Density (g/mL)	% Mass Removed	Volume Removed (mL)
D1	38.9	1.35	0.09	0.16
D2	37.4	1.33	0.09	0.16
D3	37.6	1.33	0.13	0.23
D4	37.9	1.34	0.12	0.22
D5	38.8	1.34	0.13	0.22
D6	37.6	1.33	0.10	0.17
Sample	% Volume Removed	Volume Removed (mL) per mL of Water	Compaction (%)	
D1	0.09	0.002	3.10	
D2	0.09	0.002	1.00	
D3	0.13	0.002	1.70	
D4	0.12	0.002	2.30	
D5	0.13	0.002	3.10	
D6	0.10	0.002	2.50	

Table A-5: The initial conditions and results of suffosion modeling with Dellahunt soil models D1-D6 for the second iteration.

Sample	Initial Soil Mass (g)	Water Volume (mL)	Saturated Soil Mass (g)	
D1	237.14	100	291.56	
D2	239.01	100	295.02	
D3	237.11	100	295.46	
D4	237.57	100	294.59	
D5	234.53	100	290.39	
D6	234.9	100	289.57	
Sample	Initial Soil Volume (mL)	Final Soil Volume (mL)	Dried Soil Mass (g)	Soil Removed (g)
D1	175.35	169.37	230.27	0.05
D2	179.15	176.61	231.35	0.07
D3	177.88	176.79	230.97	0.1
D4	176.79	174.08	230.98	0.09
D5	175.35	173.36	227.6	0.05
D6	176.43	175.35	229.28	0.12
Sample	Final Porosity (%)	Final Bulk Density (g/mL)	% Mass Removed	Volume Removed (mL)
D1	36.2	1.36	0.12	0.20
D2	36.1	1.31	0.13	0.22
D3	36.5	1.31	0.18	0.31
D4	36.5	1.33	0.16	0.29
D5	36.2	1.31	0.15	0.27
D6	34.4	1.31	0.15	0.27
Sample	% Volume Removed	Volume Removed (mL) per mL of Water	Compaction (%)	
D1	0.12	0.002	6.40	
D2	0.13	0.002	2.40	
D3	0.18	0.003	2.30	
D4	0.16	0.003	3.80	
D5	0.15	0.003	4.20	
D6	0.15	0.003	3.10	

Table A-6: The initial conditions and results of suffosion modeling with Dellahunt soil models D1-D6 for the third iteration.

Sample	Initial Soil Mass (g)	Water Volume (mL)	Saturated Soil Mass (g)	
D1	230.27	100	286.06	
D2	231.35	100	300.37	
D3	230.97	100	295.46	
D4	230.98	100	295.17	
D5	227.6	100	286.81	
D6	229.28	100	295.84	
Sample	Initial Soil Volume (mL)	Final Soil Volume (mL)	Dried Soil Mass (g)	Soil Removed (g)
D1	169.37	172.23	234.14	0
D2	176.61	175.53	236.04	0.01
D3	176.79	176.07	234.58	0.09
D4	174.08	176.25	234.86	0.01
D5	173.36	174.08	230.98	0
D6	175.35	173.36	233.31	0.08
Sample	Final Porosity (%)	Final Bulk Density (g/mL)	% Mass Removed	Volume Removed (mL)
D1	30.1	1.36	0.12	0.20
D2	36.6	1.34	0.13	0.22
D3	34.6	1.33	0.21	0.38
D4	34.2	1.33	0.17	0.29
D5	32.1	1.33	0.15	0.26
D6	36.1	1.35	0.18	0.32
Sample	% Volume Removed	Volume Removed (mL) per mL of Water	Compaction (%)	
D1	0.12	0.002	4.82	
D2	0.13	0.002	3.00	
D3	0.21	0.004	2.70	
D4	0.17	0.003	2.60	
D5	0.15	0.003	3.80	
D6	0.18	0.003	4.20	

Table A-7: The initial conditions and results of suffosion modeling with Dellahunt soil models D7-D12 for the first iteration.

Sample	Initial Soil Mass (g)	Water Volume (mL)	Saturated Soil Mass (g)	
D7	236.66	100	307.73	
D8	235.21	100	294.93	
D9	239.12	100	303.36	
D10	235.79	100	307.12	
D11	237.88	100	299.64	
D12	237.99	100	300.85	
Sample	Initial Soil Volume (mL)	Final Soil Volume (mL)	Dried Soil Mass (g)	Soil Removed (g)
D7	180.96	176.97	246.61	0.24
D8	180.96	174.8	244.92	0.52
D9	180.96	175.53	247.38	0.37
D10	180.96	174.98	247.79	0.3
D11	180.96	175.53	247.96	0.54
D12	180.96	176.79	247.89	0.45
Sample	Final Porosity (%)	Final Bulk Density (g/mL)	% Mass Removed	Volume Removed (mL)
D7	34.5	1.39	0.10	0.17
D8	28.6	1.40	0.21	0.37
D9	31.9	1.41	0.15	0.26
D10	33.9	1.42	0.12	0.21
D11	29.4	1.41	0.22	0.38
D12	30.0	1.40	0.18	0.32
Sample	% Volume Removed	Volume Removed (mL) per mL of Water	Compaction (%)	
D7	0.10	0.002	2.20	
D8	0.21	0.004	3.40	
D9	0.15	0.003	3.00	
D10	0.12	0.002	3.30	
D11	0.22	0.004	3.00	
D12	0.18	0.003	2.30	

Table A-8: The initial conditions and results of suffosion modeling with Dellahunt soil models D7-D12 for the second iteration.

Sample	Initial Soil Mass (g)	Water Volume (mL)	Saturated Soil Mass (g)	
D7	246.61	100	291.96	
D8	244.92	100	285.84	
D9	247.38	100	302.71	
D10	247.79	100	299.06	
D11	247.96	100	290.6	
D12	247.89	100	292.84	
Sample	Initial Soil Volume (mL)	Final Soil Volume (mL)	Dried Soil Mass (g)	Soil Removed (g)
D7	176.97	174.8	237	0.15
D8	174.8	174.08	235.33	0.01
D9	175.53	175.89	238.24	0.15
D10	174.98	175.17	236.64	0.16
D11	175.53	173.17	238.98	0.01
D12	176.79	171.37	238.28	0.07
Sample	Final Porosity (%)	Final Bulk Density (g/mL)	% Mass Removed	Volume Removed (mL)
D7	31.4	1.36	0.16	0.29
D8	29.0	1.35	0.23	0.39
D9	36.7	1.35	0.22	0.38
D10	35.6	1.35	0.19	0.34
D11	29.8	1.38	0.23	0.40
D12	31.8	1.39	0.22	0.37
Sample	% Volume Removed	Volume Removed (mL) per mL of Water	Compaction (%)	
D7	0.16	0.003	3.40	
D8	0.23	0.004	3.80	
D9	0.22	0.004	2.80	
D10	0.19	0.003	3.20	
D11	0.23	0.004	4.30	
D12	0.22	0.004	5.30	

Table A-9: The initial conditions and results of suffosion modeling with Dellahunt soil models D7-D12 for the third iteration.

Sample	Initial Soil Mass (g)	Water Volume (mL)	Saturated Soil Mass (g)	
D7	237	100	291.77	
D8	235.33	100	299.29	
D9	238.24	100	297.45	
D10	236.64	100	294.51	
D11	238.98	100	294.06	
D12	238.28	100	293.24	
Sample	Initial Soil Volume (mL)	Final Soil Volume (mL)	Dried Soil Mass (g)	Soil Removed (g)
D7	174.8	174.8	229.77	0.07
D8	174.08	174.98	228.05	0.06
D9	175.89	175.17	230.03	0.1
D10	175.17	177.34	228.42	0.06
D11	173.17	169.19	230.87	0.04
D12	171.37	174.26	230.93	0.02
Sample	Final Porosity (%)	Final Bulk Density (g/mL)	% Mass Removed	Volume Removed (mL)
D7	35.5	1.31	0.20	0.35
D8	40.7	1.30	0.26	0.45
D9	38.5	1.31	0.27	0.47
D10	37.3	1.29	0.23	0.40
D11	37.3	1.36	0.26	0.43
D12	35.8	1.33	0.23	0.41
Sample	% Volume Removed	Volume Removed (mL) per mL of Water	Compaction (%)	
D7	0.20	0.003	3.40	
D8	0.26	0.005	3.30	
D9	0.27	0.005	3.20	
D10	0.23	0.004	2.00	
D11	0.26	0.004	6.50	
D12	0.23	0.004	3.70	

Table A-10: The initial conditions and results of suffosion modeling with Elcor soil models E1-E6 for the first iteration.

Sample	Initial Soil Mass (g)	Water Volume (mL)	Saturated Soil Mass (g)	
E1	202.98	100	264.06	
E2	212.96	100	272.73	
E3	220.45	100	283.66	
E4	217.23	100	283.99	
E5	216.8	100	276.98	
E6	217.62	100	281.83	
Sample	Initial Soil Volume (mL)	Final Soil Volume (mL)	Dried Soil Mass (g)	Soil Removed (g)
E1	180.96	164.85	199.08	0.25
E2	180.96	170.1	210.91	0.27
E3	180.96	174.08	219.06	0.08
E4	180.96	175.17	216.77	0.1
E5	180.96	173.54	216.89	0.27
E6	180.96	171.91	215.23	0.13
Sample	Final Porosity (%)	Final Bulk Density (g/mL)	% Mass Removed	Volume Removed (mL)
E1	39.4	1.21	0.13	0.21
E2	36.3	1.24	0.13	0.22
E3	37.1	1.26	0.04	0.06
E4	38.4	1.24	0.05	0.08
E5	34.6	1.25	0.12	0.22
E6	38.7	1.25	0.06	0.10
Sample	% Volume Removed	Volume Removed (mL) per mL of Water	Compaction (%)	
E1	0.13	0.002	8.90	
E2	0.13	0.002	6.00	
E3	0.04	0.001	3.80	
E4	0.05	0.001	3.20	
E5	0.12	0.002	4.10	
E6	0.06	0.001	5.00	

Table A-11: The initial conditions and results of suffosion modeling with Elcor soil models E1-E6 for the second iteration.

Sample	Initial Soil Mass (g)	Water Volume (mL)	Saturated Soil Mass (g)	
E1	199.08	100	253.16	
E2	210.91	100	269.8	
E3	219.06	100	279.3	
E4	216.77	100	264.1	
E5	216.89	100	247.05	
E6	215.23	100	272.52	
Sample	Initial Soil Volume (mL)	Final Soil Volume (mL)	Dried Soil Mass (g)	Soil Removed (g)
E1	164.85	165.39	197.83	0.01
E2	170.1	172.09	209.04	0.04
E3	174.08	175.35	217.15	0.07
E4	175.17	175.17	214.04	0
E5	173.54	171.73	214.07	0.01
E6	171.91	173.72	212.83	0.02
Sample	Final Porosity (%)	Final Bulk Density (g/mL)	% Mass Removed	Volume Removed (mL)
E1	33.5	1.20	0.13	0.22
E2	35.3	1.21	0.15	0.26
E3	35.4	1.24	0.07	0.12
E4	28.6	1.22	0.05	0.08
E5	19.2	1.25	0.13	0.22
E6	34.4	1.23	0.07	0.12
Sample	% Volume Removed	Volume Removed (mL) per mL of Water	Compaction (%)	
E1	0.13	0.002	8.60	
E2	0.15	0.003	4.90	
E3	0.07	0.001	3.10	
E4	0.05	0.001	3.20	
E5	0.13	0.002	5.10	
E6	0.07	0.001	4.00	

Table A-12: The initial conditions and results of suffosion modeling with Elcor soil models E7-E12 for the first iteration.

Sample	Initial Soil Mass (g)	Water Volume (mL)	Saturated Soil Mass (g)	
E7	215.67	100	271.58	
E8	218.71	100	272.92	
E9	217.03	100	271.92	
E10	218.31	100	277.75	
E11	212.06	100	265.24	
E12	215.52	100	270.61	
Sample	Initial Soil Volume (mL)	Final Soil Volume (mL)	Dried Soil Mass (g)	Soil Removed (g)
E7	180.96	168.11	214.87	0.52
E8	180.96	172.09	219.44	0.2
E9	180.96	170.64	219.06	0.22
E10	180.96	171.37	221.63	0.35
E11	180.96	168.83	213.41	0.34
E12	180.96	168.29	217.29	0.25
Sample	Final Porosity (%)	Final Bulk Density (g/mL)	% Mass Removed	Volume Removed (mL)
E7	33.7	1.28	0.24	0.41
E8	31.1	1.28	0.09	0.16
E9	31.0	1.28	0.10	0.17
E10	32.7	1.29	0.16	0.27
E11	30.7	1.26	0.16	0.27
E12	31.7	1.29	0.12	0.19
Sample	% Volume Removed	Volume Removed (mL) per mL of Water	Compaction (%)	
E7	0.24	0.004	7.10	
E8	0.09	0.002	4.90	
E9	0.10	0.002	5.70	
E10	0.16	0.003	5.30	
E11	0.16	0.003	6.70	
E12	0.12	0.002	7.00	

Table A-13: The initial conditions and results of suffosion modeling with Elcor soil models E7-E12 for the second iteration.

Sample	Initial Soil Mass (g)	Water Volume (mL)	Saturated Soil Mass (g)	
E7	214.87	100	266.98	
E8	219.44	100	269.54	
E9	219.06	100	269.66	
E10	221.63	100	269.8	
E11	213.41	100	268.72	
E12	217.29	100	270.34	
Sample	Initial Soil Volume (mL)	Final Soil Volume (mL)	Dried Soil Mass (g)	Soil Removed (g)
E7	168.11	166.84	204.05	0.13
E8	172.09	170.46	209.27	0
E9	170.64	168.29	208.47	0.13
E10	171.37	169.92	209.43	0.02
E11	168.83	166.12	203.95	0.06
E12	168.29	169.56	207.25	0.11
Sample	Final Porosity (%)	Final Bulk Density (g/mL)	% Mass Removed	Volume Removed (mL)
E7	37.7	1.22	0.32	0.53
E8	35.4	1.23	0.10	0.16
E9	36.4	1.24	0.17	0.28
E10	35.5	1.23	0.18	0.30
E11	39.0	1.23	0.20	0.33
E12	37.2	1.22	0.17	0.29
Sample	% Volume Removed	Volume Removed (mL) per mL of Water	Compaction (%)	
E7	0.32	0.005	7.80	
E8	0.10	0.002	6.53	
E9	0.17	0.003	8.05	
E10	0.18	0.003	6.75	
E11	0.20	0.003	9.41	
E12	0.17	0.003	5.73	

Table A-14: The initial conditions and results of suffosion modeling with Elcor soil models E13-E18 for the first iteration.

Sample	Initial Soil Mass (g)	Water Volume (mL)	Saturated Soil Mass (g)	
E13	214.74	100	272.6	
E14	217.73	100	275.53	
E15	213.57	100	274.39	
E16	217.09	100	275.83	
E17	218.11	100	279.34	
E18	215.85	100	275.42	
Sample	Initial Soil Volume (mL)	Final Soil Volume (mL)	Dried Soil Mass (g)	Soil Removed (g)
E13	180.96	168.83	209.03	0.26
E14	180.96	168.11	211.79	0.21
E15	180.96	168.47	207.9	0.17
E16	180.96	171.73	212.14	0.25
E17	180.96	172.23	212.98	0.33
E18	180.96	173.36	210.33	0.15
Sample	Final Porosity (%)	Final Bulk Density (g/mL)	% Mass Removed	Volume Removed (mL)
E13	37.7	1.24	0.12	0.21
E14	37.9	1.26	0.10	0.17
E15	39.5	1.23	0.08	0.14
E16	37.1	1.24	0.12	0.20
E17	38.5	1.24	0.15	0.27
E18	37.5	1.21	0.07	0.12
Sample	% Volume Removed	Volume Removed (mL) per mL of Water	Compaction (%)	
E13	0.12	0.002	6.70	
E14	0.10	0.002	7.10	
E15	0.08	0.001	6.90	
E16	0.12	0.002	5.10	
E17	0.15	0.003	4.82	
E18	0.07	0.001	4.20	

Table A-15: The initial conditions and results of suffosion modeling with Elcor soil models E13-E18 for the second iteration.

Sample	Initial Soil Mass (g)	Water Volume (mL)	Saturated Soil Mass (g)	
E13	209.03	100	262.65	
E14	211.79	100	265.32	
E15	207.9	100	256.31	
E16	212.14	100	272.78	
E17	212.98	100	252.43	
E18	210.33	100	265.67	
Sample	Initial Soil Volume (mL)	Final Soil Volume (mL)	Dried Soil Mass (g)	Soil Removed (g)
E13	168.83	171.37	208.95	0
E14	168.11	173.17	211.58	0.04
E15	168.47	169.74	207.78	0.01
E16	171.73	168.47	211.96	0.06
E17	172.23	172.27	212.83	0.02
E18	173.36	171.73	210.37	0.02
Sample	Final Porosity (%)	Final Bulk Density (g/mL)	% Mass Removed	Volume Removed (mL)
E13	31.3	1.22	0.12	0.21
E14	31.0	1.22	0.12	0.20
E15	28.6	1.22	0.09	0.15
E16	36.1	1.26	0.15	0.25
E17	23.0	1.24	0.16	0.28
E18	32.2	1.23	0.08	0.14
Sample	% Volume Removed	Volume Removed (mL) per mL of Water	Compaction (%)	
E13	0.12	0.002	5.30	
E14	0.12	0.002	4.30	
E15	0.09	0.001	6.20	
E16	0.15	0.002	6.90	
E17	0.16	0.003	4.80	
E18	0.08	0.001	5.10	

Table A-16: Geochemical data of the soluble fraction of soils from twenty-five field infiltration sites.

Sample ID:	Ca (ppm)	Mg (ppm)	Na (ppm)	K (ppm)	CO3 (ppm)	HCO3 (ppm)	Cl (ppm)	SO4 (ppm)	TDS
1-1	2.93	0.45	0.00	51.11	0	21.97	5.05	1.10	82.61
2-1	11.17	1.04	0.00	6.54	0	130.58	15.82	28.98	194.13
3-1	13.29	0.49	0.00	5.99	0	21.97	15.90	11.75	69.39
4-1	372.91	0.11	0.00	6.22	0	6.10	15.54	683.99	1084.88
5-1	33.11	0.48	0.00	5.87	0	15.87	15.74	54.83	125.89
6-1	327.12	0.18	0.00	16.85	0	6.10	57.75	478.93	886.93
7-1	342.25	0.33	0.00	5.14	0	9.76	15.99	555.13	928.61
8-1	234.59	0.93	0.00	5.66	0	7.32	16.76	402.06	667.32
9-1	28.29	0.20	0.00	5.44	0	9.76	15.73	101.60	161.02
10-1	301.50	0.12	0.00	4.66	0	26.85	15.26	1198.79	1547.18
11-1	9.22	0.42	0.00	4.78	0	14.64	15.86	37.64	82.57
12-1	202.34	0.22	0.84	7.15	0	9.76	15.81	764.63	1000.75
13-1	329.90	0.53	0.00	0.65	0	12.20	11.70	1261.29	1616.28
14-1	184.78	0.21	0.00	0.24	0	7.32	0.00	697.02	889.57
15-1	266.47	0.12	0.00	0.00	0	6.10	0.00	1070.53	1343.23
16-1	56.38	0.28	0.00	0.44	0	14.64	24.82	218.14	314.71
17-1	261.91	0.17	0.00	0.00	0	9.76	10.74	10.87	293.46
18-1	144.53	0.16	1.07	0.00	0	9.76	0.00	1339.82	1495.35
19-1	1.82	0.15	0.31	0.00	0	23.19	0.00	1186.63	1212.11
20-1	6.03	0.29	0.00	0.00	0	29.29	11.15	15.11	61.87
21-1	4.50	0.31	0.00	0.11	0	28.07	27.98	11.34	72.31
22-1	240.80	0.15	0.00	0.00	0	15.87	11.20	18.01	286.02
23-1	40.75	0.16	0.00	0.00	0	20.75	0.00	1623.98	1685.64
24-1	2.87	0.23	0.00	0.00	0	28.07	11.05	323.14	365.36
25-1	205.57	0.11	0.00	0.00	0	19.53	11.18	0.00	236.40

VITA

Jonah D. Morris graduated from The Woodlands College Park High School in The Woodlands, Texas. He received the degree of Bachelor of Science in Geology from Stephen F. Austin State University and commissioned as a 2nd Lieutenant in the United States Army in December of 2016. In January of 2017, Jonah was admitted to the Graduate School of Stephen F. Austin State University and received the degree of Master of Science in Geology in December of 2018.

Permanent Address: 1024 Lamar
 San Antonio, TX 78202

Style manual designation: Geological Society of America

This thesis was typed by Jonah D. Morris